FABRICATION OF ANNEALED PROTON-EXCHANGED WAVEGUIDES FOR VERTICAL INTEGRATION

A Thesis

by

JACOB DOUGLAS WEBB

Submitted to the Office of Graduate Studies of
Texas A&M University
in partial fulfillment of the requirements for the degree of

MASTER OF SCIENCE

May 2011

Major Subject: Electrical Engineering

FABRICATION OF ANNEALED PROTON-EXCHANGED WAVEGUIDES FOR VERTICAL INTEGRATION

A Thesis

by

JACOB DOUGLAS WEBB

Submitted to the Office of Graduate Studies of
Texas A&M University
in partial fulfillment of the requirements for the degree of

MASTER OF SCIENCE

Approved by:

Co-Chairs of Committee, Christi K. Madsen
Ohannes Eknoyan
Committee Members, Jim Ji
Kenith Meissner
Head of Department, Costas Georghiades

May 2011

Major Subject: Electrical Engineering

ABSTRACT

Fabrication of Annealed Proton-Exchanged Waveguides for Vertical Integration. (May 2011)
Jacob Douglas Webb, B.S., Texas A&M University
Co-Chairs of Advisory Committee: Dr. Christi K. Madsen
Dr. Ohannes Eknoyan

There is a drive for improving the surface uniformity of optical waveguide devices in the photonics lab. This report focuses on the exploration of annealed proton exchange (APE) waveguide fabrication on lithium niobate crystal as a method of producing optical waveguides. These waveguides aim to have little variation in step height or surface roughness in the transition area from the waveguide location to that of the bulk crystal, providing a uniform surface amenable to vertical device integration. This is a substantial improvement over the titanium diffused waveguide process, which can have surface variations in excess of 100nm. It is anticipated that the smoother surface will enable light to couple more easily into photonic devices, such as ring resonators, as compared to the current Ti diffused waveguide process.

This work explores the design and fabrication aspects of annealed proton exchange waveguides. A review of literature on modeling hydrogen diffusion into lithium niobate is presented, as well as computer models for simulating the bidimensional fractional hydrogen proton concentration distribution. This is used to determine the change in refractive index of the waveguide needed to simulate the mode propagation and profile in the device.

Fabrication processes involved in proton exchange waveguide formation are outlined, and measurements for working devices are presented. Best case loss for current devices are 0.5 dB/cm. These samples exhibit smooth surfaces with only +-60A in variation of surface uniformity. Concluding remarks present ideas to further the work by lowering propagation losses, improving mode matching to single mode fiber, and improving the consistency of fabrication conditions.

To my family

ACKNOWLEDGMENTS

I thank God for the opportunity I have had to pursue a higher education and gain experience in a research environment with a great team. I would like to thank my mentor Dr. Christi Madsen for the projects and opportunities she has provided to me during my education at Texas A&M, as well as for her enthusiasm and encouragement in my research. I would also like to acknowledge Dr. Ohannes Eknoyan, Dr. Jim Ji, and Dr. Kenith Meissner for serving on my advisory committee, and for the advice and help they have offered me along the way. I thank Donnie Adams for introducing me to Dr. Madsen and the rest of the Photonic Signal Processing Group, as well as mentoring me along the way. I thank both Donnie and Tim Snider for training me in the lab and for being fountains of knowledge. They were always willing to share their experience. I thank the rest of the PSP group: Mehmet Solmaz, Wee-Chong Tan, Xiomin Song, Alex Xin Xia, Cage Qi Chen, Ivan Yifeng Zhou, Jae Kim, and Dwayne Macik for all of their aid, friendship, laughs, and even "man games." I would also like to thank Robert Atkins, Jim Gardner, Dennie Spears, Travis James, and the rest of the lab staff for all the help and support they offered. I thank the Defense Advanced Research Projects Agency as well as the Missile Defense Agency for the generous funding they have provided our department that has made this research possible. Last and most importantly, I would like to thank my parents and siblings for their love, support, and encouragement along the way.

TABLE OF CONTENTS

Page

ABSTRACT iii

DEDICATION iv

ACKNOWLEDGMENTS v

TABLE OF CONTENTS vi

LIST OF FIGURES ix

LIST OF TABLES xii

1. INTRODUCTION 1

2. PROTON EXCHANGE PROCESS 3

2.1 Background 3
2.2 Sample Preparation/Mask Materials 5
2.3 Modeling APE Waveguides Formed in Pure Benzoic Acid 6
2.3.1 Initial Exchange Depth Model 6
2.3.2 Anneal Depth Model 9
2.3.3 Hydrogen Concentration and $LiNbO_3$ Crystal Phases 10
2.3.4 Refractive Index Modeling 18
2.3.5 Low Loss α Phase 20
2.3.6 Mode Propagation and Mode Profile (using FimmWave) 22
2.4 Variants 26
2.4.1 Vapor Phase Proton Exchange 27
2.4.2 Reverse Proton Exchange 27
2.4.3 Soft Annealing 28
2.4.4 Alternative Proton Sources 28

3. DEVICE FABRICATION PROCEDURE 30

3.1 Overview 30
3.2 Photolithography 31
3.3 Etching 32
3.4 Proton Exchange 32

Page

3.5 Anneal Precess 34
3.6 Polishing 35
3.6.1 Polishing Procedure 36
3.7 Transmission Measurements 37
3.8 Mode Profile Measurement 39

4. APE FABRICATION RESULTS 40

4.1 Lithography Trials 40
4.1.1 Liftoff Lithography Trials 40
4.1.2 Dark Field Mask Lithography Trials with Image Reversal 41
4.1.3 Dark Field Mask Lithography Trials 43
4.1.4 Image Reversal Lithography Trials 44
4.2 Etching and Surface Roughness 48
4.3 Waveguide Transmission Measurements 50
4.3.1 Initial Trials 50
4.3.2 Series A (RC 521,522) 52
4.3.3 Series B, (RC 523,525) 53
4.3.4 Series C (RC 548, 569) 55
4.3.5 Series D (RC 529, 542, 549, 559) 56
4.4 Mode Profile Measurements 57

5. CONCLUSION AND FUTURE DIRECTION 61

5.1 More Robust Exchange Apparatus 61
5.2 Better Anneal Furnace Characterization and Calibration 62
5.3 Characterization of Benzoic Acid Diffusivity for System 62
5.4 Waveguide Mode Progile Measurement and Optimization 63
5.5 Device Integration 64
5.6 Mode Dispersion Analysis 64
5.7 Detailed Surface Inspection 65

REFERENCES 66

APPENDIX 70

Page

VITA 75

LIST OF FIGURES

Page

Figure 1.1. Images of chalcogenide glass (As_2S_3) ring resonator.. 2

Figure 2.1. Illustration of an APE waveguide with SiO_2 masking layer. 4

Figure 2.2. A) Sample is sputtered with 200nm mask material, coated in resist, and exposed to UV light exposure through negative photomask pattern. 5

Figure 2.3. During the Proton exchange process, the unmasked area of the lithium niobate is exposed to energetic hydrogen ions.. 7

Figure 2.4. A) Plot of exchange diffusion coefficient as a function of temperature.. 8

Figure 2.5. A) Plot of diffusion coefficient for anneal temperatures, x-cut crystal. 10

Figure 2.6. A) Fractional [H] vs depth plot for a variety of PE exchange depths d_e, with thermal anneal for 10.5 hours and using Howerton's diffusion constants. 13

Figure 2.7. This figure illustrates the direction of vertical and lateral diffusion of hydrogen protons in $LiNbO_3$ with a slit width of *2w*.. 14

Figure 2.8. This plot shows fractional hydrogen concentration profile, as a function of slit width *2w*. 15

Figure 2.9. At anneal start, the fractional [H] value x= 0.8 as expected, and the exchanged region is a rectangular profile of 7μmx0.427μm. 16

Figure 2.10. After only 3 minutes of anneal the concentration profile appears oblong and enters the β phase. 17

Figure 2.11. After 6 minutes of annealing the profile is still oblong, and concentration x enters the α + β phase since $x < 0.56$. 17

Figure 2.12. After 30 minutes the H^+ concentration has an elliptical distribution. 17

Figure 2.13. After 1 hour the [H] distribution is still in the lossy α + β phase. 18

Figure 2.14. After 2.5 hours the sample has been sufficiently annealed to place it in the low loss α phase meeting the requirement... 18

Figure 2.15. These figures are for the mode propagation simulation of an APE waveguide fabricated with initial exchange 20min@200C, and subsequently annealed for 4 hours at 400C. 20

Page

Figure 2.16. These simulation plots show the dependence of proper anneal time and temperature for realizing high quality, low loss waveguides in the alpha crystal phase. 21
Figure 2.17. This figure plots simulations for x-cut $LiNbO_3$ samples undergoing initial exchange in pure benzoic acid heated to 200°C, followed by thermal anneal for the time shown on the x-axis.. 23
Figure 2.18 Computer renderings of propagating TE modes.. 25
Figure 2.19. Electric field distribution representation for Ti:$LiNbO_3$ diffused waveguides as was represented by McCaughan and Murphy.. 26
Figure 3.1. The process begins with a lithium niobate sample cut into rectangular shape.. 30
Figure 3.2. The sample is then etched either by immersion in dilute hydrofluoric acid, or by reactive ion etching. 30
Figure 3.3. The photoresist layer is removed leaving only the mask layer on the sample surface, which now has channel openings etched in it. 30
Figure 3.4. The sample is cleaned and annealed at a higher temperature to diffuse the hydrogen ions into the $LiNbO_3$ substrate. 31
Figure 3.5. Lastly the SiO_2 protective layer is etched away leaving low loss waveguides with a smooth surface. 31
Figure 3.6. A) Photograph of the PE setup employing a digital hotplate, glass beaker, and insulating sleeve.. 33
Figure 3.7. Photograph of a diffusion furnace used for thermal anneal of APE waveguides. 34
Figure 3.8. Polishing setup.. 35
Figure 3.9. Sample examination.. 36
Figure 3.10. Sample end inspection under microscope.. 37
Figure 3.11. Illustration of butt coupling fibers to a waveguide on an array 37
Figure 3.12. Photograph of the LUNA OVA used for waveguide transmission characterization. 38
Figure 3.13. Schematic of the beam profiler setup 39
Figure 4.1. Liftoff lithography illustrations.. 40
Figure 4.2. Incorrect resist profile for lift-off. 41

Page

Figure 4.3. Dark field photolithography with image reversal steps. 42
Figure 4.4. Resist sidewall profile after an image reversal exposure and development. 43
Figure 4.5. Dark field photolithography steps. 44
Figure 4.6. Image reversal photolithography steps. 45
Figure 4.7. Photoresist development images. 46
Figure 4.8. Photoresist development images. 47
Figure 4.9. SiO_2 protective mask removal. 48
Figure 4.10. Measurement from 2cm length sample RC 416, featuring a 200nm SiO_2 mask, and fabricated by 30 minute exchange at 200°C, followed by a 4 hour anneal at 350°C. 51
Figure 4.11. A) This plot simulates the annealing of a PE sample fabricated by immersion in benzoic acid for 20 minutes at 200°C (d_e= 0.4478 μm).................................... 52
Figure 4.12. Series of anneal simulations created to compare times required to reach alpha phase (d_e/d_a<0.133). 55
Figure 4.13. Simulation plot showing the large influence temperature change has on anneal depth and time.. 57
Figure 4.14. Intensity profile data from ThorLabs Beam Profiler, plotted in MATLAB. 58
Figure 4.15. Beam profiler screen captures. 59
Figure 4.16. FimmWave APE waveguide simulation, intensity profile 60
Figure 5.1. Simulation of mode-mismatch in fiber to fiber coupling.. 63

LIST OF TABLES

Page

Table 2-1. Diffusion constants and activation energies for PE in x and z cut $LiNbO_3$ 8

Table 2-2. Diffusion constants and activation energies for diffusion in x and z-cut $LiNbO_3$. 10

Table 2-3. Phase boundaries for fractional hydrogen in lithium niobate. 11

Table 4-1. Surface profile readings for three SiO2 masked samples. 49

Table 4-2. RC 521, 360°C anneal 53

Table 4-3. RC 522, 360°C anneal 53

Table 4-4. RC 523, 360°C anneal 54

Table 4-5. RC 525, 360°C anneal 54

Table 4-6. RC 548, 360°C anneal 56

Table 4-7. RC 569, 360°C anneal 56

Table 4-8. Calculated values: d_e- initial exchange depth, d_a anneal depth. 56

Table 4-9. Measurement data from beam profile measurements 59

1. INTRODUCTION

The field of integrated optics focuses on creating optical devices on a chip for smaller and more robust operation. Pursuit of integrated optics stems from the advent of optical fibers for high speed telecommunications over long distances with very little transmission loss. These devices also benefit from being immune to electromagnetic interference. Integrated optical components interface with such fibers to form devices such as Mach-Zender interferometers, amplitude and phase modulators, as well as ring resonators for digital filtering. This work concentrates on the design and fabrication of waveguides, which serve as the basic building block for integrated optical devices. The annealed proton-exchange (APE) technique of forming waveguides will be explored in-depth, including benefits this technique offer in comparison to the titanium diffusion process.

The Photonics Group at Texas A&M focuses on the use of chalcogenide glass patterns to create digital filters. Optical waveguides are used to couple light from fiber optic cables into these digital filters, which are built as a secondary layer on top of the optical waveguide as shown in Figure 1.1-A. Our standard fabrication procedure utilizes titanium diffusion to create waveguides in a lithium niobate semiconductor substrate. This process involves depositing a thin strip of titanium on the $LiNbO_3$ surface where light will be guided. The device is then treated to thermal anneal at temperatures in excess of 1000 degrees Celsius for a duration of ten hours or more. The thermal anneal drives the titanium source into the $LiNbO_3$ crystal, creating a diffused concentration profile of titanium ions embedded in the substrate. The inclusion of these ions in the substrate increases the refractive index of the crystal in this region, allowing light to be guided along this path. This is analogous to a fiber optic cable which features a silicon dioxide core surrounded by a cladding with lower refractive index. This allows light to be guided with very little loss inside the fiber.

The surface of a virgin lithium niobate wafer is extremely smooth, due to a chemical polishing process performed on the material by the manufacturer. Unfortunately the Ti diffused

This thesis follows the formatting of *IEEE Transactions on Nanotechnology*

waveguide process creates an uneven surface in the guiding region, as can be seen in Figure 1.1-B. We have experienced surface non-uniformities in excess of 150nm. This is suspected to adversely affect the capacity of the waveguide to couple light into the overlaying chalcogenide glass ring resonator layer.

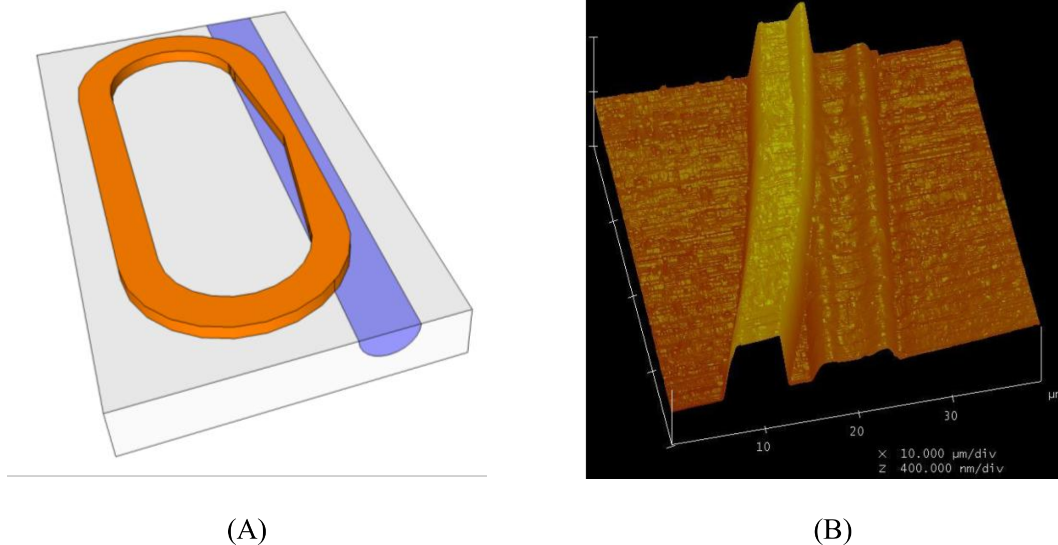

(A) (B)

Figure 1.1. Images of chalcogenide glass (As_2S_3) ring resonator. A) Computer image of ring resonator patterned on an underlying diffused waveguide. B) Atomic force microscopy image of an actual As_2S_3 ring segment (left) overlapping a diffused titanium waveguide (right).

As can be seen in the above AFM image, titanium diffusion into $LiNbO_3$ forms a ridge or bump on the waveguide surface. The annealed proton-exchange waveguide process forms guides with smooth, even surfaces that we anticipate will improve optical coupling efficiency into overlaying ring resonator layers.

This work is organized into chapters covering the design and fabrication of APE waveguides, and then discusses the results we have obtained from employing this process which is new to our lab. Concluding remarks summarize our findings, and point towards the next stages of proton exchange implementation in our creation of ring resonator filters.

2. PROTON EXCHANGE PROCESS

This section gives a brief overview of the development of the proton exchange process, including common fabrication procedures. The work focuses mainly on the annealed proton exchange (APE) process in lithium niobate, with later mention of newer processes such as RPE and HTPE. More importantly this section offers methods of modeling hydrogen diffusion into $LiNbO_3$ for both vertical and lateral directions, as well as formulations for the waveguide surface index and crystal phase. These models are combined to offer parameters requisite to simulate APE mode profile, effective index, and number of propagating modes using FimmWave waveguide solver software, by Photon Design Ltd.

2.1 BACKGROUND

The two main processes of fabricating waveguides in lithium niobate are titanium diffusion and hydrogen proton exchange. Both processes insert impurities into the $LiNbO_3$ crystal lattice. The region of the crystal containing these impurities experiences an increase in refractive index. Light can therefore be confined to this region of increased refractive index forming an optical waveguide.

Proton exchange waveguides were first observed irregularly when forming waveguides by exchange of silver-lithium or thallium-lithium in $LiNbO_3$ and $LiTaO_3$ [1]. It was found that small amounts of water were present in the $AgNO_3$ and $HTaO_3$ melts used for these experiments, and that hydrogen-lithium exchange was the actual cause of index change requisite for forming waveguides. This discovery led to the use of a variety of acids as a hydrogen proton source.

The most common acid used as a proton source is benzoic acid (C_6H_5COOH). This has been the acid of choice due to its large working temperature range, relative non-toxicity, and minimum damage to the $LiNbO_3$ crystal lattice [1]. Benzoic acid is a powdered solid at room temperature, and exhibits a melting temperature of 129°C. Jackel first reported PE waveguide formation in 1982 by submersing x-cut LiNbO3 crystals in molten benzoic acid heated to temperatures ranging from 200 to 250°C, and for times ranging from 5 minutes to 24 hours [2]. Samples were masked with a chrome or gold layer, leaving channel openings ranging from 1 to 20μm. It was found that deep waveguides could be formed relatively quickly in the unmasked areas, exhibiting a step-like refractive index profile in the exchanged area. This area underwent an increase in refractive index (Δn) of 0.12 along the extraordinary optical axis at 633nm, thus passing only the

extraordinary polarization. These waveguides encountered significant mode mismatch losses when coupled to optical fibers, and experienced additional losses due to their high change in refractive index [3]. Reports show that the ordinary index experiences either no change or a negligible negative change [1], [4].

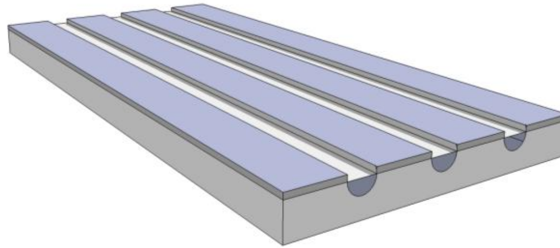

Figure 2.1. Illustration of an APE waveguide with SiO_2 masking layer. This sample features 3 waveguide channels. The semicircular features on the end represent the diffused hydrogen profile.

Subsequent experiments involved exchanging z-cut LiNbO3 crystals in benzoic acid, also creating a change in extraordinary refractive index, therefore passing only the transverse magnetic mode. Exchanging y-cut crystals would also change the extraordinary ordinary axis, but this is not commonly performed as benzoic acid actually etches $LiNbO_3$ in the y-direction [2]. Monitoring PE waveguides showed decreased electro optic coefficient, and instability in the index profile due to the out diffusion of hydrogen [5]. It was later found that PE samples undergoing thermal treatment would have a stable diffused refractive index profile, with restoration of the electrooptic properties [3].

Suchoski et al found that reducing the hydrogen content in the exchanged region created stable waveguides with low loss, restored electrooptic coefficient, and better mode matching to single mode fibers [3]. The reduction in hydrogen could be performed either by adding small quantities of lithium benzoate to the melt, or by annealing the samples in a furnace for a few hours. While the use of dilute lithium melts increases the quality of PE waveguides, it also suffers from significant increases in the amount of time required for device fabrication. Jackel also reports that maintaining proper melt composition is not trivial, and that small variances can greatly affect the fabrication process [1]. Due to the lengthy increase in exchange time inherent to the

dilute melt method, thermal anneal was chosen by Suchoski for his experiments on fabricating high quality, low loss waveguides for operation at telecomm wavelengths. This work will therefore choose to focus on the fabrication of annealed proton exchange (APE) waveguides due to the simplicity and rapidity of the fabrication process.

2.2 SAMPLE PREPARATION/MASK MATERIALS

Prior to exchange a thin film of masking material is used to protect the crystal surface, exposing only those areas where it is desired that waveguides be formed. This is somewhat analogous to masking or stenciling an area with tape or other protectant prior to spray painting the surface so that the paint only sticks to the surface in the exposed areas.

Evaporation, chemical vapor deposition, and magnetron sputtering are a few methods of fabricating a protective mask layer. Metal masks such as aluminum, titanium [4], and tantalum are commonly used, as well as silicon dioxide [6], [7], [8]. These mask layers are typically between 50 and 200nm in thickness, and must have good coverage (few to no pinholes) in order to protect the bulk crystal surface.

Mask layers are patterned using photolithography, followed by either a liftoff or etching step to remove mask material from the channel waveguide location. The following series of images illustrates a positive lithography process that can be used to pattern the mask material.

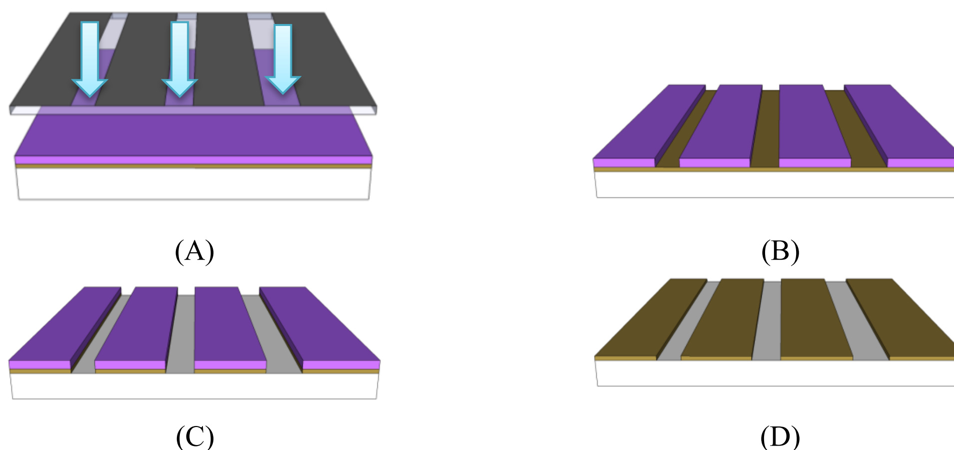

Figure 2.2. A) Sample is sputtered with 200nm mask material, coated in resist, and exposed to UV light exposure through negative photomask pattern. B) Positive image is developed forming channels in the resist, resembling the photomask pattern. C) Masking layer is etched in HF solution until LiNbO3 surface is exposed. D) Photoresist is stripped, leaving mask material (SiO2 or Ti).

The masked material with patterned waveguide locations can then be immersed in benzoic acid melt to introduce H^+ ions beneath the $LiNbO_3$ surface. After the exchange process one can remove the mask prior to annealing; commonly with a wet etchant such as hydrogen fluoride. In the case of SiO_2 protective mask Korkishko and Federov have found that leaving the SiO_2 mask layer on the sample during the anneal process can improve waveguide quality (reduce loss) by preventing pitting that can occur with LiO_2 out diffusion at high temperatures [8]. Once the mask is removed, the sample features a smooth surface that has been virtually unperturbed by the relatively low temperature APE process.

2.3 MODELING APE WAVEGUIDES FORMED IN PURE BENZOIC ACID

Due to its ubiquitous employment in proton exchange waveguide fabrication, the modeling portion of this work will focus solely on waveguides formed using pure benzoic acid as a source of hydrogen protons. These modeling methods should be used as guidelines, keeping in mind that fabrication results can vary significantly based upon proton source and melt composition [2].

Modeling APE waveguides requires an understanding of the diffusivity of hydrogen protons in $LiNbO_3$. Using known diffusion models one can compute d_e, the initial exchange depth of a PE waveguide for a specific crystal cut. Then one can compute d_a, the anneal diffusion depth. The total diffusion depth d_t would then be the sum of these two quantities. Using these parameters one can generate a model of the hydrogen concentration profile in the waveguide region, and subsequently form an expression for the change in refractive index due to the presence of hydrogen. Finally this expression for refractive index in the guiding region can be analyzed using a number of methods such as the effective index method, WKB (Wentzel-Kramers-Brillouin), or FEM (finite element mesh) in order to determine the effective index for different guided modes. This work will use FimmWave software to evaluate the mode propagation.

2.3.1 Initial Exchange Depth Model

In order to form a proton exchange waveguide, the surface must first be prepared by depositing a mask layer with the purpose of protecting the bulk $LiNbO_3$ surface. Metal and SiO_2 masks are typically used, and deposited using evaporation, sputtering, or CVD, and have typical thicknesses ranging from 50 to 200nm. Waveguide channel openings are then patterned on the mask surface. The mask is removed from this area exposing the $LiNbO_3$ surface. When immersed in benzoic acid melt, the hydrogen protons are introduced into the surface of the sample only in the unmasked region, where they are exchanged with lithium ions. This diffusion

occurs only in the vertical direction, with negligible horizontal diffusion. The result is a rectangular or step-like area of concentrated hydrogen near the surface of the sample. The dimensions of this exchanged area are the mask width w, and exchange depth d_e as pictured below.

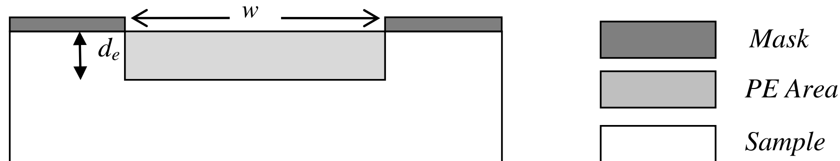

Figure 2.3. During the Proton exchange process, the unmasked area of the lithium niobate is exposed to energetic hydrogen ions. The hydrogen diffusion at these low temperatures is anisotropic, and often modeled as only occurring in the vertical direction. With zero lateral diffusion, the resulting hydrogen concentration profile is rectangular shaped, forming a step index waveguide.

The PE diffusion of hydrogen ions is a function of exchange time and temperature. One must first determine the exchange diffusion coefficient $D_e(T)$ at a specific temperature T. The working range is between the melting temperature of 129°C, and evaporating temperature of 249°C.

$$D_e(T) = D_e^0 e^{-(Q/R*T)} \tag{1}$$

$$d_e = 2\sqrt{D_e t_e} \tag{2}$$

From this exchange diffusion coefficient, one may estimate the exchange depth d_e for a given time and temperature using equation 2. Here Q is the activation energy, R is Boltman's constant, and t_e is the proton exchange time. Values for these constants are listed in. Table 2-1.

The following charts depict the diffusion coefficient and exchange depth for PE performed in x-cut $LiNbO_3$ using pure benzoic acid. The diffusion coefficient calculations span a BA melt temperature range of 160 to 249°C. The exchange depth calculations shown are for PE waveguides formed in pure benzoic acid for the following temperatures: 180, 200, and 220°C. The exchange time span ranges from 1 to 60minutes, and shows the high temperature sensitivity of exchange depth. It is worth noting that the exchange depth is highly sensitive to temperature.

For instance it would take 40min at a temperature of 180°C to obtain an exchange depth of 0.4μm. An exchange at 220°C could achieve this same depth in a much shorter time of roughly 7 minutes. These figures were generated using the constants in Table 2-1, which were reported by Almeida [9].

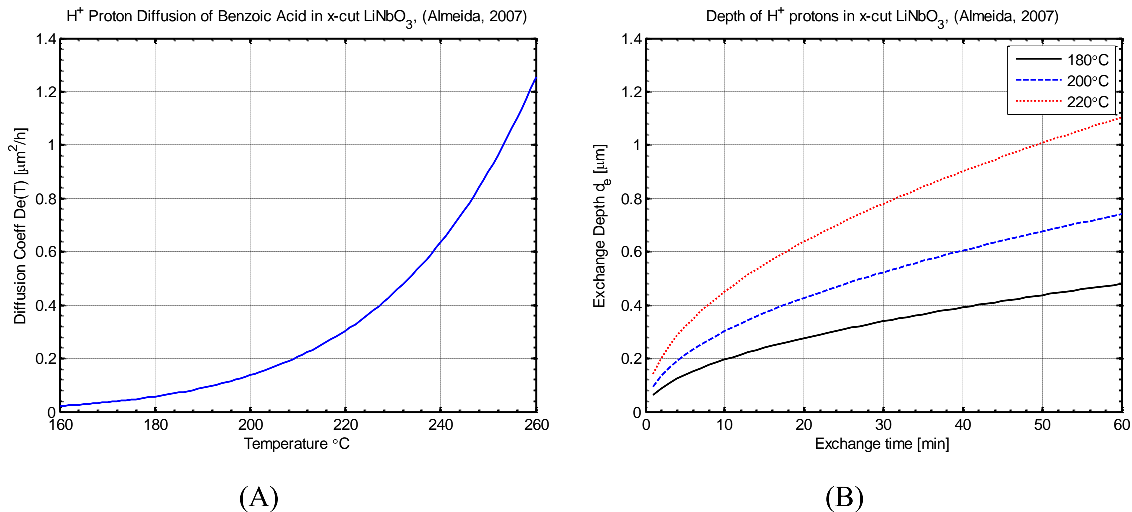

(A) (B)

Figure 2.4. A) Plot of exchange diffusion coefficient as a function of temperature. This plot is generated from constants published by Almeida. It is noteworthy that changes in temperature have a significant effect on diffusion rate. B) Plot of exchange depth vs time for a series of temperatures spanning from 180 to 220°C.

From these charts one can see the influence of temperature on exchange depth. It is therefore important that the PE setup maintain a stable temperature during the exchange process in order to reach the desired exchange depth d_e.

Table 2-1**.** Diffusion constants and activation energies for PE in x and z cut $LiNbO_3$
Reference 1 from Almeida, and reference 2 for literature comparison in his report.

	D_0 (x10^8)	ΔQ
X-cut$_1$	0.48	77.4
X-cut$_2$	1.50	79.3
Z-cut$_1$	2.94	87.1
Z-cut$_2$	7.8	7.7

D_e	Initial exchange diffusion coefficient
D_o	Diffusivity
t_e	Exchange time
d_e	Initial exchange depth
T	Exchange temperature [K]
Q	Activation energy [eV/mol]
R	Boltzman's constant 8.314472 [J/mol*K]

2.3.2 Anneal Depth Model

Following the initial proton exchange, samples undergo thermal treatment with no proton source, which leads to a broadening of the hydrogen proton concentration and refractive index. This anneal typically takes place at temperatures in the range of 300 to 450°C. As is the case with exchange depth, anneal depth d_a is also a function of exchange time and temperature. Following the same method as for the exchange depth, one can determine the anneal diffusion coefficient $D_a(T)$ at a specific temperature T. The diffusion coefficients are different for x and z-cut $LiNbO_3$, and therefore calculations must be performed using data for the specified crystal cut.

$$D_a(T) = D_a^0 e^{-(H/K*T)} \tag{3}$$

From this exchange diffusion coefficient, one may estimate the anneal depth d_a for a given time and temperature using equation 4. Here H is the activation energy, K is Boltman's constant, and t_a is the thermal anneal time. Values for these constants are listed in Table 2-2.

$$d_a = 2\sqrt{D_a t_a} \tag{4}$$

The following charts depict the diffusion coefficient and anneal depth for x-cut $LiNbO_3$. These figures were generated using the empirical diffusion data presented by Almeida, and included here in table [#2]. The temperature vs time plot in particular shows the importance of proper furnace calibration when annealing samples for a target anneal depth. According to this plot, a 2um anneal depth can be obtained by a 10 hour anneal at 350°C, or less than an hour for a furnace temperature of 400°C.

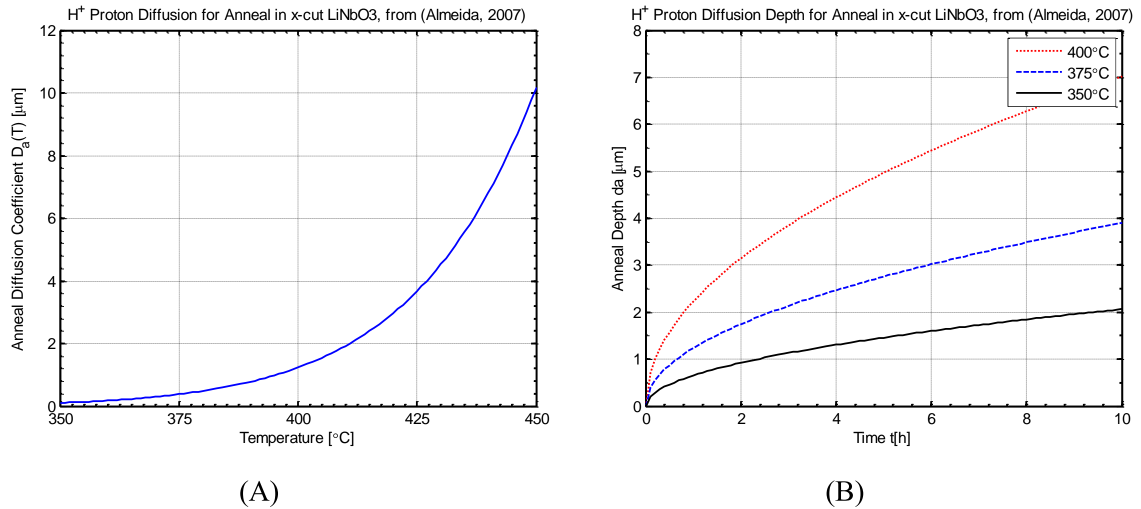

(A) (B)

Figure 2.5. A) Plot of diffusion coefficient for anneal temperatures, x-cut crystal. B) Plot of anneal temperatures 350, 375, and 400, showing the increase in anneal depth with time.

Table 2-2. Diffusion constants and activation energies for diffusion in x and z-cut $LiNbO_3$. Reference 1 from Almeida [9], and reference 2 for literature comparison in his report.

	$D_0\,(x10^{12})$	ΔH
X-cut$_1$	22.0	77.4
X-cut$_2$	1.50	79.3
Z-cut$_1$	2.94	87.1
Z-cut$_2$	7.8	7.7

D_a Thermal anneal diffusion coefficient
D_{ao} Anneal diffusivity
d_a Anneal depth
t_a Anneal time
T Anneal te pe ature [K]
H Activation energy [eV]
R Boltzman's constant 8.617387x10^{-5} [eV*K]

2.3.3 Hydrogen Concentration and $LiNbO_3$ Crystal Phases

As was mentioned earlier, for the PE process the change in refractive index in $LiNbO_3$ is due to the introduction of hydrogen ions into the crystal lattice. This exchange reaction, as reported by Howerton, Burns, et al [10] is described by the following formula:

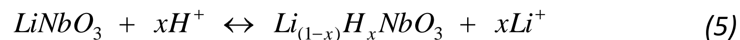

$$LiNbO_3 + xH^+ \leftrightarrow Li_{(1-x)}H_xNbO_3 + xLi^+ \quad (5)$$

The x on the right hand side of the equation represents the fractional hydrogen concentration in the exchanged region. Variations of this value determine the phase of the $LiNbO_3$ crystal in the exchanged region. The phase varies with fractional H concentration as follows:

Table 2-3. Phase boundaries for fractional hydrogen in lithium niobate.

Phase	**Fractional [H] value**
α	$x \leq 0.12$
α + β	$0.12 \leq x \leq 0.56$
β	$0.56 \leq x \leq 0.75$
β+ $HNbO_3$	$x \geq 0.75$

These phases were determined by X-ray diffraction, and reported in reference [10]. The boundaries in this chart follow the phase definitions established in Table 2-3. Howerton and Passaro, in separate reports [10], [11], use a value of $x = 0.8$ for the entire exchanged region immediately following PE in pure benzoic acid, analogous to the solubility concentration used in diffusion calculations. As the sample is annealed, the variable x follows the hydrogen concentration at the waveguide surface, which decreases as the protons are diffused further into the substrate. As the surface concentration decreases, the surface change in refractive index Δn also decreases as shown in the figure. Those waveguides attaining alpha phase exhibit low changes in refractive index comparable to that of single mode fiber, and exhibit favorably low propagation loss. Further discussion on α phase waveguides can be found in subsections 2.3.3.1 and 2.3.5.

There are now many more known crystal phases in $LiNbO_3$ that are outside the scope of the proposed APE model. A comprehensive report of these phases, with the intent of aiding in the optimization of fabrication parameters, is presented by Korkishko and Federov [12].

2.3.3.1 Hydrogen Concentration Model as a Function of Depth

The distribution formula below from Howerton describes the fractional concentration of hydrogen in the direction of anneal depth (which is represented here as the y-direction, where y=0 at the $LiNbO_3$ surface).

$$C_H(y,t_a) = \frac{Ax_e}{2}\left[erf\left(\frac{d_e+y}{d_a}\right)+erf\left(\frac{d_e-y}{d_a}\right)\right] \qquad (6)$$

A is the atomic density of $LiNbO_3$, and x_e is the fractional hydrogen concentration in the anneal region. Evaluating equation (6) at the surface where y= 0 yields an expression for the surface concentration, x_a:

$$Ax_a = C_H(0,t_a) = Ax_e erf\left(\frac{d_e}{d_a}\right) \qquad (7)$$

For small values of d_a in comparison to d_e, the profile becomes a step or rectangular function, representative of the initial exchange concentration profile. As the sample is annealed for longer times or at higher temperatures, the profile reflects a Gaussian distribution Howerton gives by evaluating the error function in (6):

$$C_y(y,t_a) = \frac{Ax_e d_e}{\sqrt{\pi}d_a}e^{\left(\frac{-y^2}{d_a^2}\right)} = Ax_a e^{\left(\frac{-y^2}{d_a^2}\right)} \qquad (8)$$

Using both sides of equation 8, evaluated at the surface y=0, Howerton produces a relation for surface concentration x_a dependent upon exchange and anneal depths.

$$x_a = \frac{Ax_e d_e}{\sqrt{\pi}d_a} \qquad (9)$$

For α phase waveguides having a target surface concentration $x_a \le 0.12$, and given the initial exchange fractional concentration $x_e = 0.8$, equation 9 can be transformed into a guideline useful for creating low-loss α phase proton exchange waveguides:

$$\frac{d_a}{d_e} \geq 7.5, \quad \text{or} \quad \frac{d_e}{d_a} \leq 0.133 \qquad (10)$$

See subsection 2.3.5 for further elaboration on α phase waveguides.

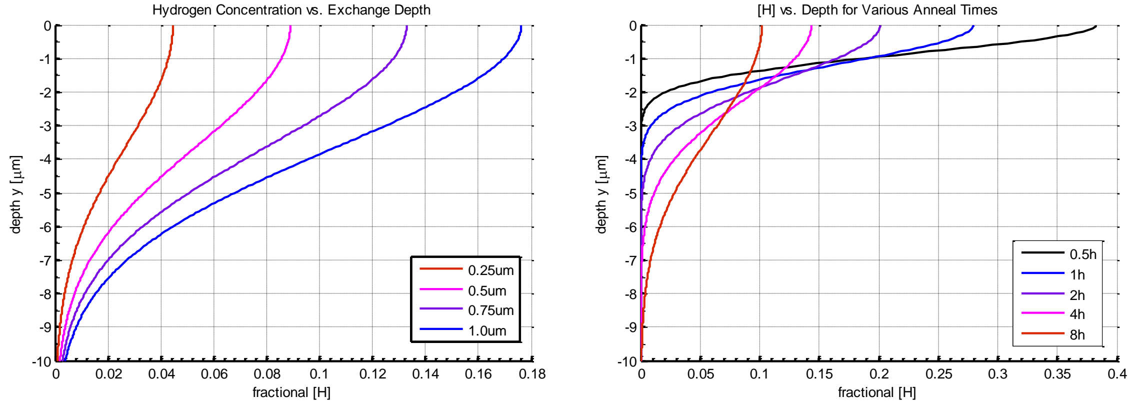

(A) (B)

Figure 2.6. A) Fractional [H] vs depth plot for a variety of PE exchange depths d_e, with thermal anneal for 10.5 hours and using Howerton's diffusion constants. B) Fractional [H] vs. depth for a variety of anneal times, assuming initial PE exchange depth d_e of 0.5um

2.3.3.2 Hydrogen Concentration Model as a Function of Width

This section will describe relations used to model the horizontal concentration of H protons at various anneal times. These calculations rely on mask width opening, crystal cut, and diffusion time and temperature. The figure below represents the masked sample with waveguide slit width opening *2w*.

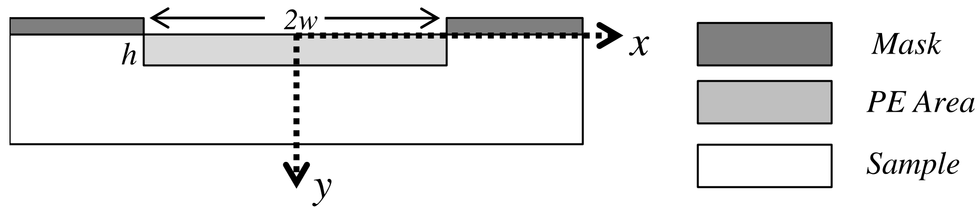

Figure 2.7. This figure illustrates the direction of vertical and lateral diffusion of hydrogen protons in $LiNbO_3$ with a slit width of *2w*.

The y-direction represents the depth, or vertical diffusion direction calculated in the previous section. The x-direction represents the lateral, or horizontal diffusion direction. For an x-cut $LiNbO_3$ substrate this lateral diffusion direction corresponds to the crystal z-direction, and diffusion coefficients should thus be chosen for the z-direction. Equations 3 and 4 should be used in conjunction with the diffusion constants given in Table 2-2 to determine the magnitude of diffusion in this outward direction, d_h. The fractional H concentration is given by the following formula, which has been slightly modified from Almeida in order to keep a consistent coordinate system [9].

$$C_H(x,t_a) = \frac{C_0}{2}\left[erf\left(\frac{w+x}{d_h}\right)+erf\left(\frac{w-x}{d_h}\right)\right] \qquad (11)$$

A sample plot from equation 11 is shown below.

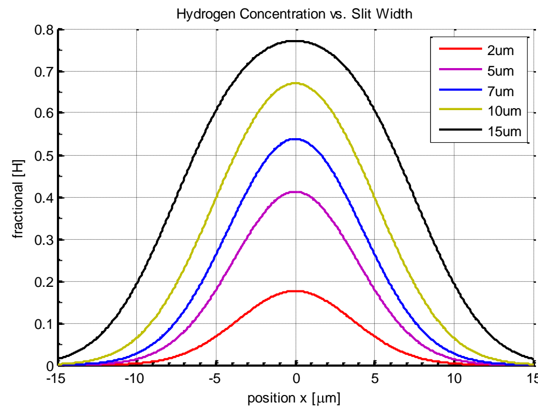

Figure 2.8. This plot shows fractional hydrogen concentration profile, as a function of slit width *2w*. The simulation assumes an anneal time of 10.5 hours at a temperature of 350C. Larger slit widths yield higher concentration profiles compared to the narrower ones, since they have a greater initial H proton source.

While it will not be explored further in this work, it is important to note that the waveguide width will affect the concentration of hydrogen ions in the substrate with greater widths exhibiting higher [H]. Increased [H] results in a greater change in refractive index Δn. The choice of waveguide width therefore offers a degree of control over the waveguide index, which can improve mode confinement. Further exploration of the subject is featured in Il'ichev's reference [4].

2.3.3.3 Bidimensional Concentration Model

Creating an accurate model of hydrogen concentration in a proton exchange waveguide requires knowledge of the diffusion of H protons in both the x and y directions. The previous sections establish a formulation of the H concentration as a function of diffusion depth and width. This section combines the two relations from equations 6 and 11 in order to create a bidimensional H concentration profile that can be used for subsequent refractive index modeling and mode propagation simulation.

This formula is similar to one used by Almeida, but has been modified to in order to keep coordinates consistent in this work [9].

$$C_H(x, y, t_a) = \frac{C_0}{4}\left[erf\left(\frac{h+y}{d_v}\right) + erf\left(\frac{h-y}{d_v}\right)\right]\left[erf\left(\frac{w+x}{d_h}\right) + erf\left(\frac{w-x}{d_h}\right)\right] \quad (12)$$

Here d_v is the diffusion in the *y* direction, corresponding to the direction of the crystal cut. This value was previously represented as d_a by Howerton. The initial proton exchange height *h* is equivalent to d_e used by Howerton. The mask width opening is 2w, and horizontal diffusion occurs in the x direction as shown in Figure 2.7. If modeling an x-cut, y-propagating sample then x-cut coefficients from Table 2-2 would be used for modeling the vertical diffusion, while z-cut coefficients would be used to model the horizontal diffusion. The temperature dependent diffusion coefficient for each direction is calculated by equation 3, and the depth d_v or width d_h of that equation is an Arrhenius relation dependent upon time and temperature, and can be determined by equation 4.

The figures below depict a simulation run in MATLAB using these equations to visualize the distribution of H protons in lithium niobate at several stages of the APE process. The color intensity in the diffused region correlates to the fractional H concentration at each anneal time, being normalized to the peak concentration for each individual plot. In order to properly interpret the [H] of each anneal time increment, one must examine the colorbar scale for each time plot. This simulation assumes a 20 minute exchange has been performed in pure benzoic acid heated to 200°C, forming an initial exchange depth d_e of 0.427μm. Mask opening width *2w* is 7μm, and anneals are performed in a furnace heated to 400°C.

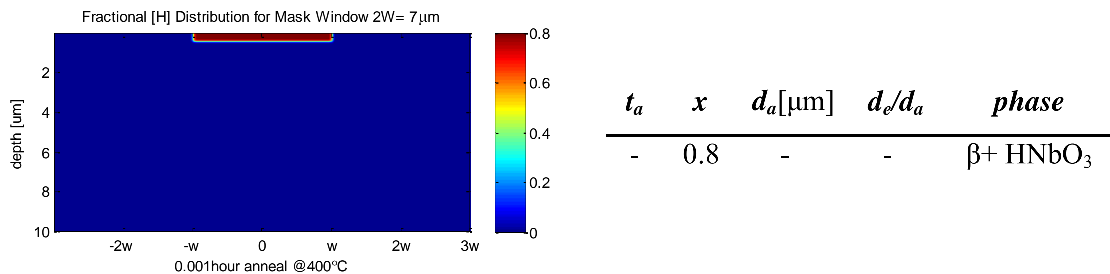

t_a	x	d_a[μm]	d_e/d_a	phase
-	0.8	-	-	β+ $HNbO_3$

Figure 2.9. At anneal start, the fractional [H] value *x*= 0.8 as expected, and the exchanged region is a rectangular profile of 7μmX0.427μm.

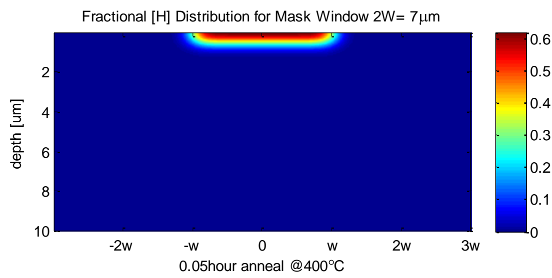

t_a	x	d_a[μm]	d_e/d_a	*phase*
0.05h	0.62	.497	0.860	β

Figure 2.10. After only 3 minutes of anneal the concentration profile appears oblong and enters the β phase.

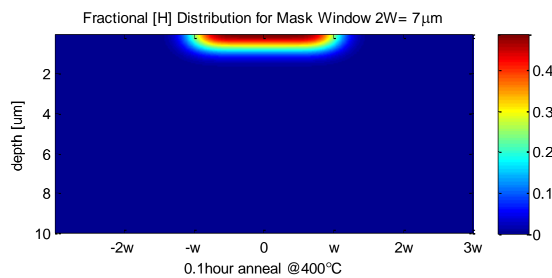

t_a		d_a [μm]	d_e/d_a	*phase*
0.1h	0.49	0.702	0.609	α + β

Figure 2.11. After 6 minutes of annealing the profile is still oblong, and concentration x enters the α + β phase since $x < 0.56$.

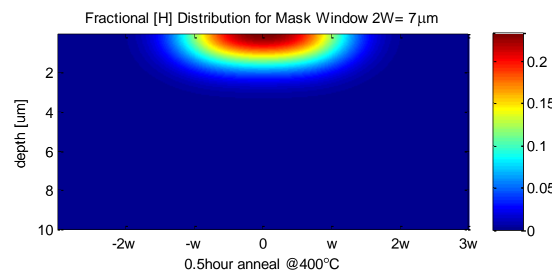

t_a	x	d_a [μm]	d_e/d_a	*phase*
0.5h	0.23	1.570	0.272	α + β

Figure 2.12. After 30 minutes the H^+ concentration has an elliptical distribution.

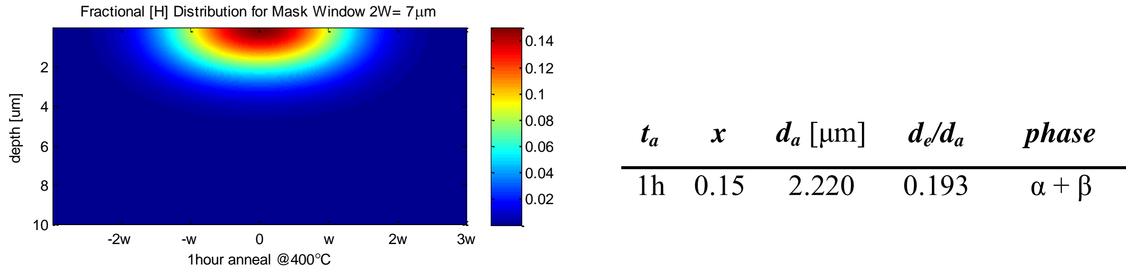

t_a	x	d_a [μm]	d_e/d_a	*phase*
1h	0.15	2.220	0.193	α + β

Figure 2.13. After 1 hour the [H] distribution is still in the lossy α + β phase.

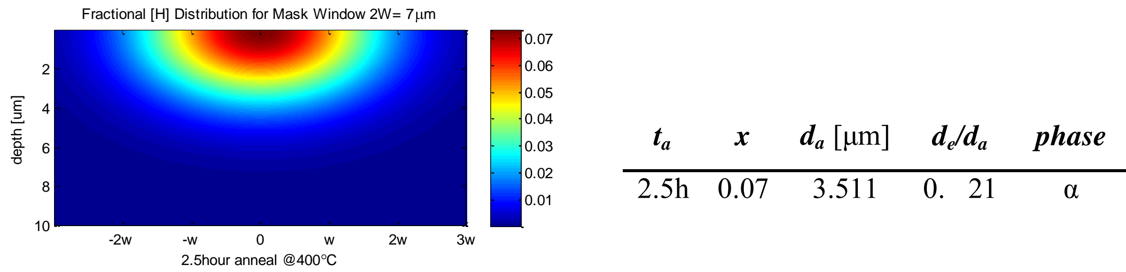

t_a	x	d_a [μm]	d_e/d_a	*phase*
2.5h	0.07	3.511	0. 21	α

Figure 2.14. After 2.5 hours the sample has been sufficiently annealed to place it in the low loss α phase meeting the requirement

2.3.4 Refractive Index Modeling

Once the concentration profile has been determined, one may estimate the refractive index as a function of H concentration. There have been many methods used to perform this estimate, and Passaro offers a comprehensive summary of these schemes [11]. Most assume a linear relationship between H concentration and change in refractive index. Howerton models the refractive index change by modifying the concentration equation 6 to be:

$$\Delta n_e(y,t_a) = \frac{\Delta n_e}{2erf\left[\frac{d_e}{d_a}\right]}\left[erf\left(\frac{d_e+y}{d_a}\right)+erf\left(\frac{d_e-y}{d_a}\right)\right] \tag{13}$$

Almeida represents the same relation [9] as:

$$\Delta n_e(y,t_a) = \frac{\Delta N_{pp}}{2}\left[erf\left(\frac{d_e+y}{d_a}\right)+erf\left(\frac{d_e-y}{d_a}\right)\right] \tag{14}$$

where ΔNpp is the peak change in index at the waveguide surface, which is a constant value depending only upon wavelength. Passaro reports a few additional schemes from existing literature, which calculate the change in index differently for each crystal phase. He then proposes his own scheme for determining the change in index uniquely applicable to α or α + β phase waveguides exhibiting a fractional H concentration of less than 0.16:

$$\Delta n_{\alpha} = \left(0.3226C + 0.183C^2\right)e^{-7.14C} \quad \text{for C} \leq 0.16 \tag{15}$$

Passaro devised this equation by fitting experimental data on concentration versus refractive index change, and shows in his report that his scheme fits the experimental data better than 5 competing schemes [11].

Finally, the refractive index of bulk lithium niobate at room temperature can be calculated as a function of wavelength using the following modified Sellmeier equation from reference [13]:

$$\begin{aligned} n_o^2 &= 4.9048 - \frac{0.11768}{0.04750 - \lambda^2} - 0.027169\lambda^2 \\ n_e^2 &= 4.5820 - \frac{0.099169}{0.04432 - \lambda^2} - 0.021950\lambda^2 \end{aligned} \tag{16}$$

I have found Passaro's non-linear index equation to be more useful than the Almeida's linear index expression when using FimmWave optical software. For my simulations I have combined Almeida's bidimensional concentration profile with Pissaro's index [13] relation to calculate the change in refractive index at the waveguide surface. This maximum change occurs at the location x=0,y=0. Example plots are found below. The value of N_{PP} used is 0.08 for 1531nm light, as per [9],and [6], and $LiNbO_3$ substrate exhibits a refractive index of n_e= 2.1386149 calculated from Eq. (16).

(A) (B)

Figure 2.15. These figures are for the mode propagation simulation of an APE waveguide fabricated with initial exchange 20min@200C, and subsequently annealed for 4 hours at 400C. The images depict the two dimensional mode profile as found with FimmWave waveguide modeling software. A) Simulation using Almeida's refractive index relation. B) Simulation using Pissaro's refractive index relation.

Simulation A was run using Almeida's linear concentration to index conversion, and leads to a very low Δn value. This leads to a low effective index value n_{eff}= 2.138609, just below that of the $LiNbO_3$ bulk. This shows as poor mode confinement, and a significant portion of the optical mode is radiated into the substrate, though in reality the mode would not exist since its effective index is less than that of the substrate.

Simulation B uses identical exchange and anneal fabrication steps, but makes use of Pissaro's relation for refractive index as a function of fractional hydrogen concentration. By comparison, the effective index n_{eff}= 2.139525 is higher in this model than that of the bulk index, showing mode confinement favorable to that of simulation A.

2.3.5 Low Loss α Phase

This section is dedicated to the design of alpha phase waveguides, exhibiting low propagation loss as previously touched on in subsection 2.3.3.1.

Howerton conducted a series of experiments on six samples to observe the hydrogen concentration and subsequent guiding behavior in annealed proton exchange waveguides [10]. These samples were exchanged in benzoic acid for 15 minutes at a temperature of 190°C ($D_e(T)$= 0.14μm^2/h), yielding an initial exchange depth of 0.38μm. The samples were individually annealed at temperatures ranging from 300 to 375°C for 3 hours in order that each

sample have a different anneal depth value d_a. The variety of increasing anneal depths could have also been accomplished by annealing the samples at a constant temperature, but for successively longer time periods. The author included empirical values for index change *Δn,* fractional hydrogen concentration *x*, anneal depth d_a, de/d_a ratios, and optical loss for these waveguides. This data shows that PE-only waveguides are in the β+ $HNbO_3$ phase due to their high fractional H concentration. Waveguides in this phase exhibit a large change in refractive index and encounter considerable propagation loss. As the anneal depth is increased, fractional hydrogen concentration decreases and samples pass through the β and α + β intermediary phases. The reduction in hydrogen reduces the refractive index, but propagation losses increase significantly. When sufficient anneal has been performed, the alpha phase condition $d_e/d_a \leq 0.133$ is met, and the samples exhibit low propagation loss as desired. This data offers an excellent gauge for expected APE waveguide performance with respect to crystal phases and exchange/anneal depths.

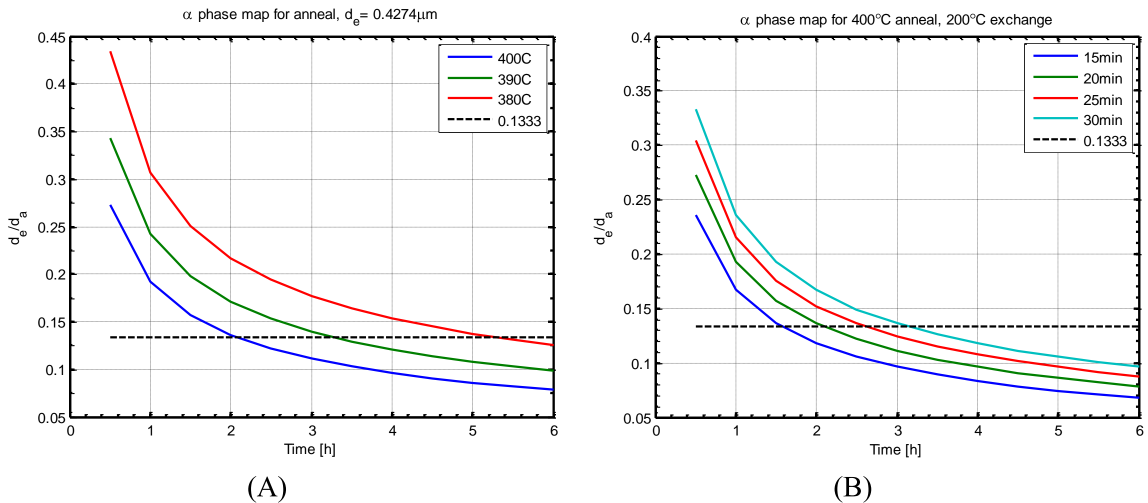

Figure 2.16**.** These simulation plots show the dependence of proper anneal time and temperature for realizing high quality, low loss waveguides in the alpha crystal phase. Each figure plots anneal temperature against the d_e/d_a criterion proposed by Howerton, as outlined in subsection 4.2.3. A) Computations for a variety of anneal temperatures ranging from 380 to 400°C. This plot assumes an initial PE for 20min@200C, for an initial depth d_e of 0.427μm. B) Computations for a series of waveguides annealed at a constant temperature of 400°C . This series is initially exchanged in pure benzoic acid for times ranging from 15 to 30 minutes at a melt temperature of 200°C.

The above graphs plot the d_e/d_a value for a variety of temperatures, with dashed line indicating the alpha phase transition (where $d_e/d_a <= 1.333$, as indicated by horizontal dashed line). Figure 2.16.A shows how alpha phase is reached more quickly by increasing the anneal temperature. A 20°C decrease in furnace temperature from 400°C requires a significant increase in anneal time for the APE waveguide to reach the alpha phase (2 hours to 5 hours). Figure 2.16.B shows the effects of exchange time on reaching the alpha phase. It should be no surprise that the shorter the proton exchange time t_e, the smaller exchange depth d_e. These samples fabricated by shorter exchange time reach alpha phase more quickly than those fabricated to a greater exchange depth when anneal time remains constant.

2.3.6 Mode Propagation and Mode Profile (using FimmWave)

Design of high quality, low loss waveguides requires matching the waveguides to the fibers that will be used to couple light into and out of the device. APE waveguides exhibit an asymmetric refractive index profile, as seen in the previous section. This asymmetry is due to the top-down fabrication process, along with the inherently anisotropic diffusion coefficients. Single mode fiber, on the other hand, has a symmetric Gaussian index profile in both the x and y directions. This section is dedicated to designing APE waveguides to match coupling fibers as best as possible.

Standard Corning SMF-28 fiber exhibits a mode field diameter (MFD) of 10μm at 1531nm. In order to produce low-loss waveguides, it is therefore important to design waveguides exhibiting a MFD as close as possible as that of the fiber. The degree to which the waveguide's mode profile differs from this fiber mode profile determines the mode miss-match loss of the system.

There are a few factors which affect the mode profile diameter of the waveguide, namely the waveguide width and depth. This work focuses mostly on waveguide depth, and a more comprehensive examination on the waveguide width is found in Il'ichev's reference [4]. It is outside the scope of this work to analyze mathematical models for optimizing the waveguide MFD. One will rely instead on using FimmWave computer aided design software to determine the waveguide MDF based upon a variation of input parameters.

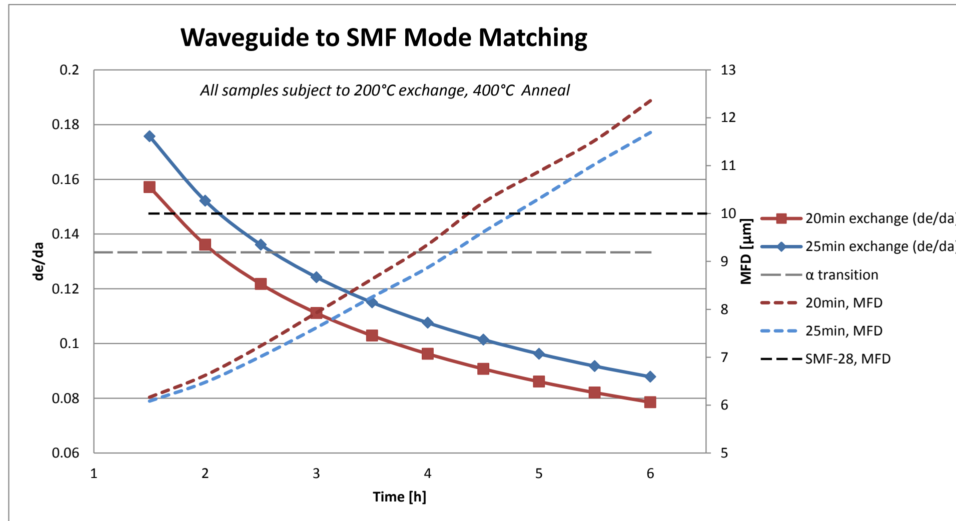

Figure 2.17. This figure plots simulations for x-cut $LiNbO_3$ samples undergoing initial exchange in pure benzoic acid heated to 200°C, followed by thermal anneal for the time shown on the x-axis. All calculations made using diffusion constants reported by Almeida [9]. These samples featured a 7µm chanenel width, and were exchanged for 20 and 25 minutes (d_e= 0.427µm, 0.478µm). The downward sloping, solid lines plot the de/da ratio for these exchange depths as a function of anneal time. The upward sloping dashed lines represent the mode field diameter of each sample as calculated in FimmWave. Horizontal dashed lines indicate the alpha phase boundary, and 10um mode filed diameter of Corning single mode fiber at 1531nm. This plot shows that samples fabricated in similar conditions will attain the low propagation loss alpha phase well before the mode size is comparable to that of standard single mode fiber.

The above chart shows how crystal phase and mode profile are influenced by anneal depth (which in itself is a function of anneal temperature and time, see subsection 2.3.2). The samples attain α phase after anneal times beyond 2 hours. Though a sample may attain the low loss α phase, it is important to remember that this is low propagation loss only. There are still coupling losses incurred during sample measurement, which increase as the waveguide mode field deviates from that of the coupling fibers. The upward sloping trends on this plot show how further anneal enlarges the waveguide MFD until it eventually intersects the10.7µm MFD of the single mode fiber reference [14]. At this 2 hour mark, where the sample fabricated by exchange in BA for 20min at 200°C reaches α phase, it has an MFD of approximately 6.5µm. Such a mismatch between this waveguide and the single mode fiber is sure to produce substantial coupling losses. According to this simulation the sample would need to be annealed for approximately 4.5 hours in order to reach a mode size comparable to that of the SMF-28 fiber. It is also worth noting that the mode field diameter is increasing at a rate of approximately 2µm/hr

at this particular temperature. A lower anneal temperature should be chosen if greater control over mode diameter is desired.

For analysis, the simulation parameters from an x-cut sample exchanged for 25min@200°C, and annealed for 3hours at 400°C, crossing into the α phase are examined in FimmWave. FimmWave requires the following input parameters in order to simulate the waveguide intensity mode field : waveguide width w, change in surface index Δn, vertical diffusion d_v , and lateral diffusion d_y. The vertical diffusion is the total diffusion d_t, which is the sum of the exchange depth d_e and the anneal depth d_a. The refractive index is calculated using Pissaro's method, based upon the H concentration distribution of the waveguide.

The following code is the output From MATLAB and FimmWave:

MATLAB output:
Exchange depth: 0.477800um
da: 3.845677um
Vertical Diffusion: 4.323477
Horizontal Diffusion: 5.574520
Substrate index: 2.138615 at 1.531um
de/da: 0.124243
Surface [H]-> x= 0.038264
dnP: 0.0096

FimmWave output:
$1/e^2(x)$= 9.24um
$1/e^2(y)$= 8.28um
n_{eff}= 2.1402

MFD= 7.62um

The refractive index model in FimmWave was set to anisotropic, with only a change value input for the x direction. The solver was then set to use FMM solver, type Semivec TE and with a maximum of 2 modes. The program generated the graphical intensity profiles seen in Figure 2.18. The mode was then plotted as seen in Figure 2.18 to determine the MFD. The plotter gives the $1/e^2$ intensity mode width in both the x and y directions (one can alternatively inspect the 1/e plot for electric field to obtain the same dimension). Despite this being an asymmetric profile, one can calculate the MFD by taking the square of the product of these quantities. For a good match with this anisotropic mode, the $1/e^2$ width will exceed that of SMF in one direction, and be less than the SMF in the other direction.

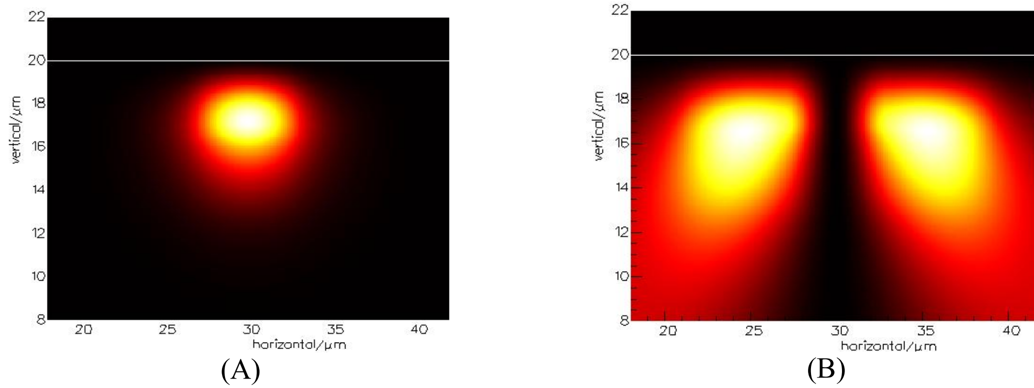

Figure 2.18 Computer renderings of propagating TE modes. A) This is a rendering of the first propagating mode in the APE waveguide. It exhibits good confinement, and an asymmetric shape with slightly larger diameter in the horizontal direction. B) This 2nd order TE mode rendering shows weak confinement.

The MFD here is significantly smaller than that of a singlemode fiber. The fiber mismatch η can be determined from the following equation, which is a solution of the mode overlap integral for diffused waveguides by McCaughan and Murphy [15].

$$\eta = 2 * \frac{\left[\left(\frac{1}{a^2}+\frac{1}{\sigma_1{}^2}\right)^{-1/2}+\left(\frac{1}{a^2}+\frac{1}{\sigma_2{}^2}\right)^{-1/2}\right]^2}{a^2\sigma_3(\sigma_1+\sigma_2)\left[\frac{1}{a^2}+\frac{1}{\sigma_3{}^2}\right]} \quad (17)$$

Here a is the fiber mode radius, σ_i is the mode 1/e radius of the E_x distribution of the TE waveguide, and is taken as is shown in the following image. The term σ_3 comes from the symmetric horizontal distribution, while σ_1 and σ_2 come from the asymmetric vertical distribution; σ_1 being the smaller of the two.

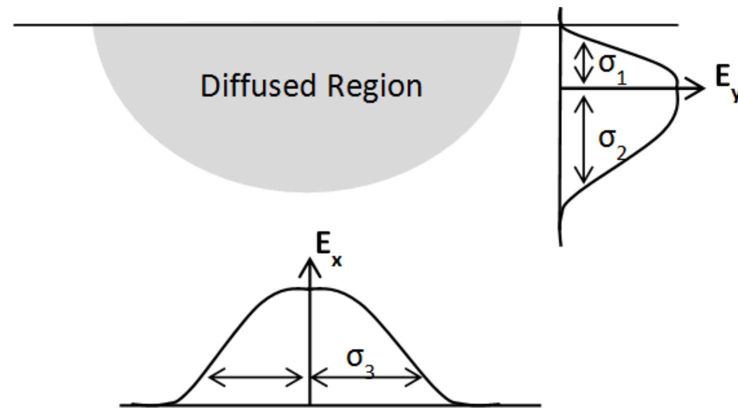

Figure 2.19. Electric field distribution representation for Ti:$LiNbO_3$ diffused waveguides as was represented by McCaughan and Murphy [15]. The sigma terms are used in conjunction with equation 16 to determine fiber to waveguide mode mismatch. These illustrations and equation can also be applied to APE waveguides, which exhibit the same anisotropic field distribution.

Once the coupling mismatch coefficient η is known, finding the coupling loss is a trivial exercise.

$$coupling\ loss = -10\log_{10}(\eta) \qquad (18)$$

From 1/e analysis in FimmWave: σ_1= 2.2um, σ_2= 4.05um, σ_3= 9.249um/2, η = 0.8497, and the coupling loss per fiber connection is 0.7074dB. By examining Figure 2.17 one can see that an anneal time in the range of 4 to 5 hours would be better suited to match the mode of the SMF-28 fiber. Additional simulations in MATLAB and FimmWave can be run until an optimal solution is found.

2.4 VARIANTS

Many other methods of PE waveguide fabrication exist which either employ alternative proton sources, or variations on the exchange process. Among these are soft proton exchange (SPE), reverse proton exchange (RPE), high temperature proton exchange (HTPE), and vapor phase

proton exchange (VPE). This section will give an overview of these processes, including a short summary of alternative proton sources.

2.4.1 Vapor Phase Proton Exchange

Vapor phase proton exchange involves heating the benzoic acid source to temperatures in excess of 250°C. This was first reported by Rams and Cabrera in 1998 [16]. The acid vapor was prevented from escaping by placing the acid and sample in a sealed ampoule system with hourglass shape. The acid was placed at the bottom, and the sample in the top. The ampoule was heated to the desired temperature and then turned over so that the acid and sample would react. Waveguides are fabricated using this technique in a matter of hours, and require no further anneal steps. While these guides are β phase, they exhibit low propagation loss and less perturbation of electrooptic coefficient in comparison to waveguides fabricated using the APE process. Z-cut crystals fabricated using the VPE process also exhibit second harmonic generation efficiency, while this ability is lost in x and y cut VPE waveguides [16].

2.4.2 Reverse Proton Exchange

The APE process creates an asymmetric refractive index profile, exhibiting a peak value at the waveguide surface. Reverse proton exchange (RPE) is an additional process used to bury the refractive index below the waveguide surface. This is achieved this by re-introducing lithium into an already exchanged $LiNbO_3$ region. The end result is less scattering from surface imperfections, and lower fiber to waveguide coupling losses due to a more symmetric mode profile, and higher conversion efficiency in non-linear processes due to better mode overlap [17], [18]. Xie et al report an increase of parametric gain by a factor of greater than 2 for optical parametric generator (OPG) frequency converters employing periodic poled lithium niobate (PPLN) waveguides fabricated by RPE versus those fabricated by APE.

Korkishko et al first demonstrated reverse exchange in metal ion exchanged waveguides, and subsequently in PE waveguides by using $LiNO_3$ melt [18]. Jackel later suggested use of lithium benzoate and mixed nitrates as possible lithium sources. Nitrate mixes must only contain small amounts of $LiNO_3$ in order to avoid surface damage. Benzoic acid and lithium benzoate

mixtures may be used, but in order to maintain melt stoichiometry it is recommended to perform the exchange in a sealed environment since the two substances evaporate at different rates [17].

To fabricate an RPE waveguide one must first form an APE waveguide, with peak [H] at the waveguide surface. During the RPE process lithium is re-introduced into the surface, out diffusing the hydrogen there. The resultant concentration profile (and consequently the index profile) has a lower peak value than that of the original APE waveguide, with the peak concentration below the waveguide surface. This creates a buried waveguide with a mode profile exhibiting greater symmetry than that of an APE waveguide. This improves mode coupling to SMF-28 fiber, which has a symmetric Gaussian index distribution in the x and y axes.

Korkishko offers a variety of melt compositions and fabrication methods in his comprehensive report on RPE fabrication, which would be a good starting point for anyone interested in this technique [18].

2.4.3 Soft Annealing

Soft anneal is a low temperature anneal used to stabilize the refractive index of a PE only waveguide, prior to thermal anneal. It also ensures that the PE only waveguide is in a single crystal phase, rather than the multiple phases indicated by Howerton. Castaldini reports that a soft anneal process increases the exchange depth by an average of 1.5, and if a 1um thick waveguide is desired then an SA should be performed for 10hours at 212°C. The author also reported increased stability only when turning off the furnace and allowing the sample to cool over a period of hours while still in the furnace. As an example, this process is used by Bamford et al in fabricating a mid-IR laser spectrometer on periodically-poled lithium niobate [19].

2.4.4 Alternative Proton Sources

Aside from benzoic acid, many other hydrogen sources have been explored for use in fabricating PE waveguides. Among those commonly used are phosphoric acid, stearic acid, and a combination of benzoic acid diluted with lithium benzoate.

Stearic acid, first proposed by Pun, offers the advantage of being inexpensive, non-toxic, noncorrosive, and exhibits a much higher boiling point of 361°C [20]. Pun reports that stearic acid exhibits a lower diffusion coefficient than both benzoic acid and phosphoric acid at the same temperature, which can lead to greater control over PE depth d_e. This method generates a step refractive index profile similar to that of PE performed in benzoic acid, and would thus require additional thermal anneal to reach alpha phase.

Korkishko et al report forming α phase waveguides in $LiNbO_3$ and $LiTaO_3$ by exchanging in a mixture of stearic acid and lithium stearate [21]. This process is performed at high temperatures and referred to as high temperature proton exchange (HTPE).

El Hadi et al report a similar process of forming graded α phase waveguides in $LiNbO_3$ by exchanging in benzoic acid diluted with lithium benzoate [22]. This type of exchange, commonly referred to as soft proton exchange (SPE) or dilute melt proton exchange (DMPE), is carried out in a sealed ampoule in temperatures in excess of 300°C. The graded index waveguides are only produced when the lithium benzoate dilution ratio ranges from 2.6 to 5%. Values lower than this create a step-like profile which require additional anneal to reach alpha phase. While direct creation of α phase waveguides in one step offers an advantage over the multiple steps for the APE process, the benefits of reduced steps are negated by increased fabrication time which can be multiple days [23], [3]. Advantages to the system also include preservation of nonlinearity properties as well as domain inversion [24].

3. DEVICE FABRICATION PROCEDURE

This section is dedicated to the various processes used to fabricate annealed proton exchange waveguides. It would be of particular interest to those new to waveguide fabrication, or others who are working on similar processes.

3.1 OVERVIEW

The following series of images illustrates the general APE waveguide fabrication procedure.

Illustrations of Fabrication Procedure

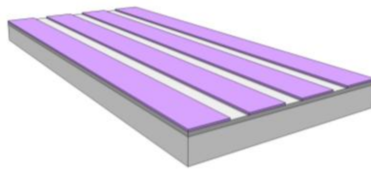

Figure 3.1. The process begins with a lithium niobate sample cut into rectangular shape. A thin masking layer, such as SiO2, is deposited on the sample surface. A layer of photoresist is then applied and patterned to protect the areas where waveguides will not be formed.

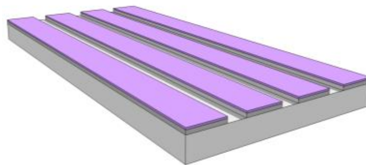

Figure 3.2. The sample is then etched either by immersion in dilute hydrofluoric acid, or by reactive ion etching. Only the masking layer is etched. The channel openings in the resist have now been etched away so that only bare LiNbO3 is seen in these channels

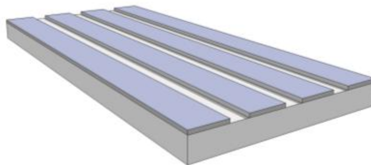

Figure 3.3. The photoresist layer is removed leaving only the mask layer on the sample surface, which now has channel openings etched in it. The sample is immersed in benzoic acid to exchange H ions through the channel openings into the exposed crystal surface.

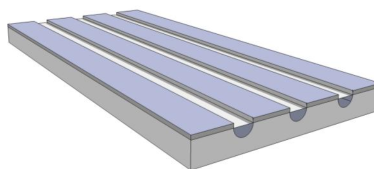

Figure 3.4. The sample is cleaned and annealed at a higher temperature to diffuse the hydrogen ions into the $LiNbO_3$ substrate.

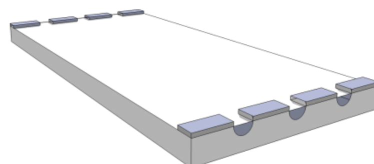

Figure 3.5. Lastly the SiO_2 protective layer is etched away leaving low loss waveguides with a smooth surface.

3.2 PHOTOLITHOGRAPHY

The Phototonics Lab at Texas A&M University uses micro-scale photolithography to transfer patterns from reference masks onto semiconductor samples, mainly waveguide arrays and ring resonators. Our setup employs a Karl Suss MA6 contact-mask aligner with peak ultraviolet spectrum of 365nm, commonly referred to as an i-line exposure aligner. The desired pattern is designed using CAD software such as L-edit. The mask begins as a simple a plate of quartz glass that has been chrome metalized on one side. The CAD file is sent to a mask manufacturer who takes this design and imprints it onto the mask by selectively removing portions of the chrome layer where it is desired that light be transmitted. The sample is then spin-coated with a photosensitive compound (photoresist), and subsequently baked on a hotplate to evaporate the majority of solvents in the photoresist. Then using the aligner the reference mask is placed in contact with the sample. Next the UV-exposure time is set and a flood of ultraviolet light passes through the chrome-free regions of the quartz mask. The pattern is completed by immersion of the sample in an aqueous developing solution for an empirically determined duration of time. When using a positive photoresist, the exposed areas of resist dissolve in the developing solution, while the remaining (unexposed) areas resist are polymerized and remain.

Exposure dose is a critical part of photolithography. The intensity of the aligner can be measured with a photometer, and used to calculate the time required to reach the desired dose. For example if a 60mJ/cm^2 dose is required, and the intensity meter is reading 6mW/cm^2, one would simply divide the dose by the intensity to determine the exposure time required, 10 seconds.

Greater detail on the photolithography processes used for APE fabrication can be found in section 4.1.

3.3 ETCHING

Two main forms of etching are used in the lab: wet and dry. Wet etching involves immersing the sample in an etchant solution that will slowly remove the target material. Dry etching employs a much more complicated setup that operates under vacuum and uses a combination of physical and chemical interactions to remove material. While either one will work for APE processing, RIE etching produced fewer problems due to the fact that the etch is only in the vertical direction. Wet etching attacks exposed surfaces in an isotropic fashion which can be problematic when forming channels in the material. As the etchant digs deeper into the surface it begins to etch also in the lateral direction which can increase waveguide openings to a value larger than that intended.

Etching channel openings in a typical sample with 200nm thick SiO_2 mask will finish in 1 minute when using 1:30 dilute HF or buffered HF. RIE etch takes longer, 3min 30s, but this is a reasonable tradeoff for the amount of control one gains with the dry etching process.

3.4 PROTON EXCHANGE

Because the ion exchange rate is temperature dependent, one must ensure that the temperature remains stable during the proton exchange process. Other groups have used heating mantles [2], heated oil baths [9], [10], or sealed ampoules [25], [26], in order to regulate the reaction temperature. Available equipment was used to assemble an exchange setup comprising of a digitally controlled hotplate with magnetic stirrer and thermocouple probe. It proved

challenging to attain a temperature sufficiently high and stable for the proton exchange process, but in the end it proved to be an effective means of implementation.

Initial trials focused on raising the acid to the desired temperature of 200°C. The acid is in a powder form at room temperature, and melts at 129°C. A small quantity of powdered benzoic acid was placed into a 100mL beaker and heated. The hotplate had no difficulties reaching the melting point of the acid (129°C), but could not attain a stable acid temperature above 160°C. Two adjustments helped to increase the temperature another 15°C. The first is to cover the acid beaker with aluminum foil, keeping any vapors in the glass beaker. The second is to decrease the air flow of the fume hood by keeping the splash guard sufficiently open. Despite these efforts it was still impossible to attain a temperature higher than 175°C. It was obvious that there was a large amount of heat loss in the system, thus preventing it from reaching the desired temperature. The setup needed to be insulated.

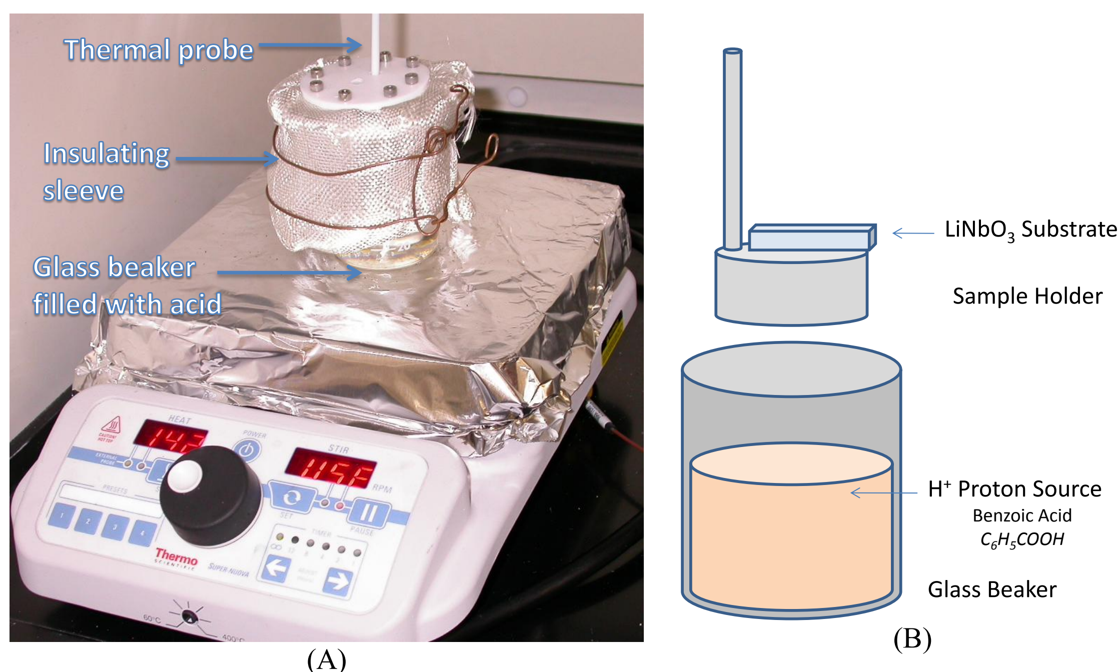

Figure 3.6. A) Photograph of the PE setup employing a digital hotplate, glass beaker, and insulating sleeve. The sleeve is a custom piece made using bulk silica fibers lined with fiberglass weave. B) Illustration of the beaker where the PE reaction takes place. The sample holder in this image is actually attached to the PTFE lid of the insulating sleeve.

The solution was to create an insulating sleeve and lid for the acid beaker. This sleeve was crafted from woven fiberglass mat stuffed with fiberglass insulation, and a polytetrafluoroethylene (PTFE) disc was attached and used as the lid. These materials were chosen due to their abilities to withstand high temperatures. The PTFE could reach temperatures of 260°C without deformation, and the silica fiberglass could exceed 1000°C. With the insulating sleeve in place, temperatures as high as 220°C were obtained in the acid setup, and were quite stable at the desired 200°C set point.

3.5 ANNEAL PROCESS

Proton exchanged waveguides formed in pure benzoic acid are inherently unstable. PE waveguides encounter additional losses when coupled to single mode fiber due to mode-index mismatch between the step-index profile of guides fabricated in pure acid and the Gaussian mode-profile of the fiber. A high temperature anneal step is commonly used to restore stability to the waveguide and diffuse the hydrogen protons, thereby reducing propagation and mode-mismatch losses.

Figure 3.7. Photograph of a diffusion furnace used for thermal anneal of APE waveguides.

Annealing is performed in a high temperature diffusion furnace. The furnace is basically a glass tube surrounded by a high power heating coil. Samples are place on a ceramic “boat” and then inserted into the center of the furnace where the temperature is the most stable.

Common PE anneal temperatures range from 300 to 450°C. These temperatures are significantly lower than those required by titanium diffused waveguide fabrication, demanding anneal temperatures in excess of 1000°C and times on the order of 10 hours. The diffusion rate of hydrogen in lithium niobate is temperature dependent and follows an Arrhenius function, which is discussed in greater detail in subsection 2.3.2.

All APE waveguides have been fabricated with fresh breathing air from a compressed source fed into the furnace. Results from various annealing times are found in subsection 4.3.2.

3.6 POLISHING

Samples ends must be polished prior to measurement. Uniform waveguide ends are desired, and provide the lowest loss. This section gives an overview of the polishing equipment and procedures used for APE fabrication at Texas A&M University.

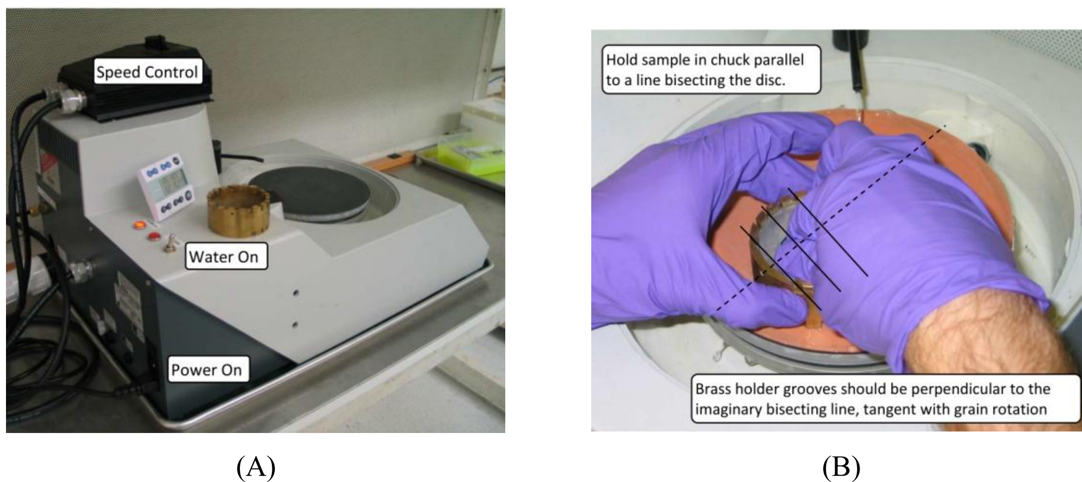

Figure 3.8. Polishing setup. A) The polishing machine consists of a magnetic spindle disc with water drip. Spin speed is varied using the controller. B) Sample being polished with orange disc (15um grain). Sample must be held perpendicular to the circular direction of rotation in order to ensure a uniform polish. Dashed line represents the direction of the sample edge being polished. Solid lines are tangential to the direction of rotation, and are the desired direction for pad/$LiNbO_3$ interaction.

Samples initially have extremely rough edges, a result of the dicing process used to form the 2x2cm substrates from a round $LiNbO_3$ wafer. After the exchange and annealing processes have been accomplished, samples should be polished using the following procedure.

3.6.1 Polishing Procedure

- **Orange Rough Polish Disc** (15.0 µm): 2-3min @ 70RPM. Check surface under microscope to ensure that waveguides extend all the way to the sample ends. Also ensure that waveguide end has minimal chipping. Then check sample end under microscope to ensure uniform grain pattern. Repeat if needed.

- **Brown Med-Fine Polish Disc (3.0 µm):** 2min @ 50RPM. Check sample end under microscope to ensure no large/deep grains. Repeat if needed.

- **White Super Fine Polish Disc** (0.5 µm): 1min30 @ 30RPM. Check and ensure no grooves remain where waveguide will be measured.

- Repeat with opposite side of sample.

(A)

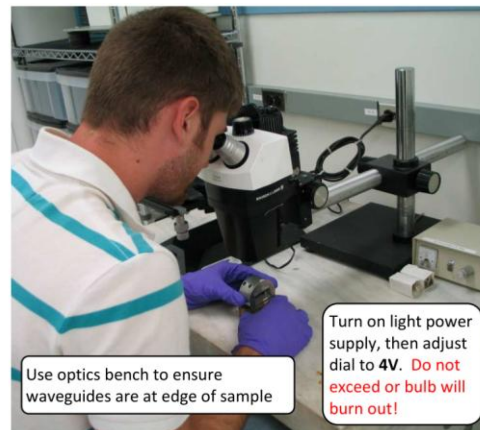

(B)

Figure 3.9. Sample examination. A)This image shows a waveguide sample surface. The edge of this sample is rough, a product of the dicing saw used to cut $LiNbO_3$ wafers into rectangular samples. Waveguide edges should be polished to remove this roughness and ensure the channel guides extend completely to the sample end. B) Optics bench used to examine the samples while still in the polishing chuck.

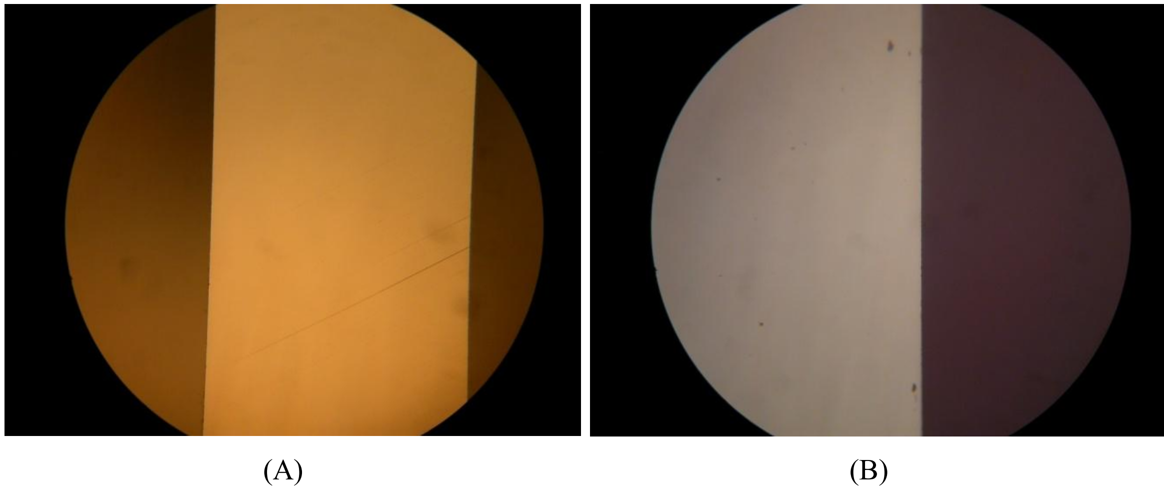

(A) (B)

Figure 3.10. Sample end inspection under microscope. A) Sample features a deep scratch on end facet and requires additional polishing. B) Photograph of a good polish. There are some specs from grit, which should be removed with soap and water.

3.7 TRANSMISSION MEASUREMENT

The waveguide transmission spectrum is characterized using the LUNA Optical Vector Analyzer. This device contains a broadly swept spectrum laser of telecomm wavelength light, and an optical receiver. Waveguide interface is performed by fiber butt coupling, and use of index matching gel. After proper alignment, the laser source is scanned over the spectrum to characterize the transmission loss as a function of wavelength for each device.

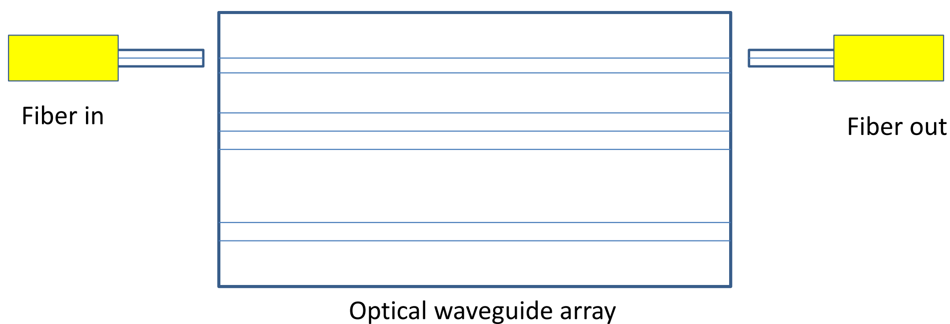

Figure 3.11. Illustration of butt coupling fibers to a waveguide on an array

A translation stage is used in conjunction with a microscope to align the fibers as close as visually discernable to the waveguide end locations. The swept wavelength source is input to one end of the waveguide, while the output is connected to a photodetector. Fine adjustments in fiber location in vertical and lateral directions are made until maximum power is delivered to the photo detector. The output power is then routed to the LUNA receiver for measurement.

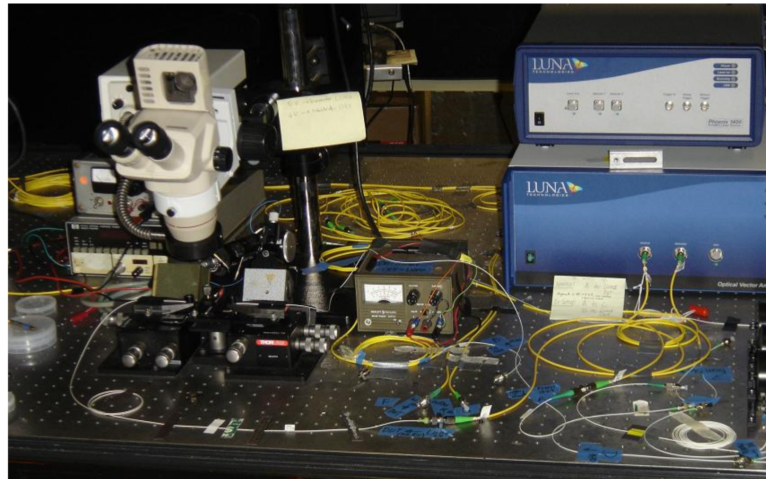

Figure 3.12. Photograph of the LUNA OVA used for waveguide transmission characterization.

Measurements and example scans are found in the next chapter which discusses fabrication results.

3.8 MODE PROFILE MEASUREMENT

The mode profile is measured using the ThorLabs Beam Profiler. This setup (depicted in Figure 3.13) uses a fiber laser to couple light into one end of the waveguide, with a lens on the opposing side used to focus the outgoing light onto the beam profiler. The profiler has a USB output, and interfaces with a computer running beam profiler software. One can then visualize on screen the mode intensity profile of the waveguide in the x and y directions. The MFD in each direction is calculated as the width between the $1/e^2$ crossing points for the normalized intensity profile. The fiber mismatch can be calculated using the formulas listed in subsection 2.3.6.

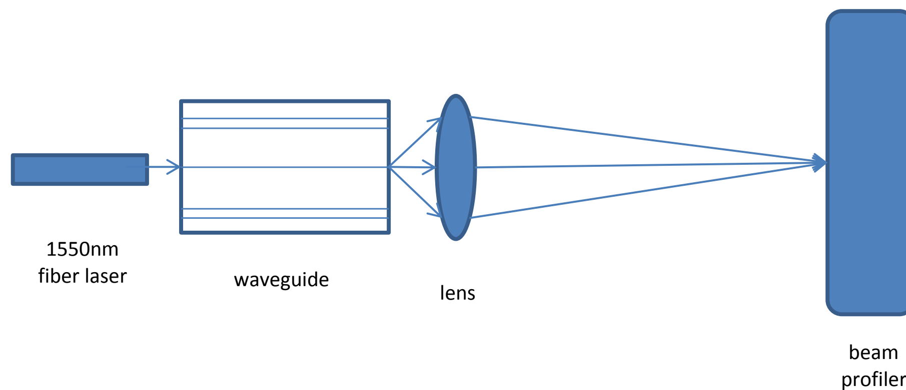

Figure 3.13. Schematic of the beam profiler setup

4. APE FABRICATION RESULTS

This section presents work that has been performed on APE waveguide fabrication. It covers the actually lithography process which was quite tricky from the beginning. It then includes results from surface profile measurements and optical loss.

4.1 LITHOGRAPHY TRIALS

This section reports on the types of lithography trials performed in preparation for proton exchange process. A variety of techniques were tried to accommodate for different masks using positive or negative images. This section would be of particular interest to anyone who is new to photolithography.

4.1.1 Liftoff Lithography Trials

The first trials employed an existing mask pattern used in titanium-diffused waveguide fabrication. This mask was transparent except for the regions in which the waveguides were to be formed. Positive resist was spin-coated onto the bare $LiNbO_3$ substrate, which was then baked and afterward exposed by mask aligner. When developed, strips of resist remained in the waveguide locations. The samples were then coated with 95nm of titanium using the EMMACO magnetron sputtering system. They were then put in acetone to dissolve the resist and lift off the titanium covering the waveguide regions.

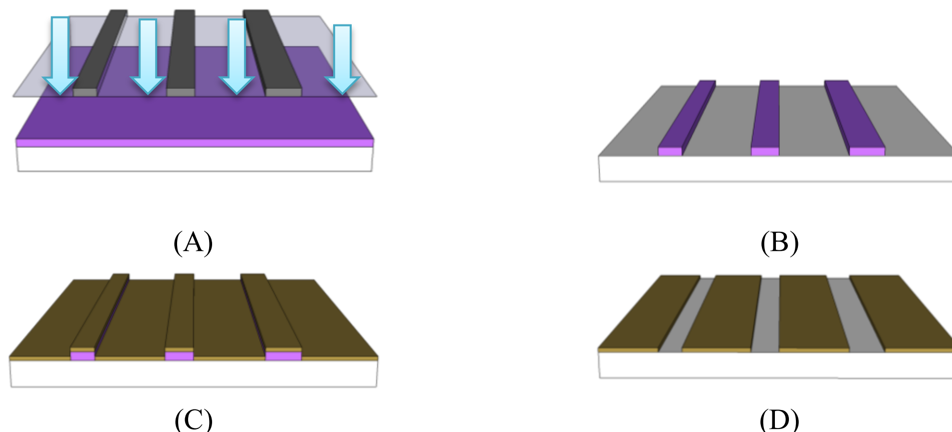

Figure 4.1. Liftoff lithography illustrations. A) UV light exposure through photomask pattern makes the exposed photoresist more soluble in developer solution. B) After development only the masked resist regions remain. C) Sputtered Ti layer covers entire sample. When soaked in solvent the resist is attacked and dissolved from the sides, lifting off the overlaying Ti. D) Remaining Ti layer is now the reverse image of the photomask.

The titanium proved impossible to lift off. It is probable that this results from the geometry of the resist profile. If the resist profile slopes outward, then the sputtered film which is deposited in a direct vertical direction can form a blanket layer that forms up and over the resist strips. The sample is therefore covered in a solid layer of the sputtered material, impervious to photoresist solvents, as is pictured in Figure 4.2.

Figure 4.2. Incorrect resist profile for lift-off. A) Positive resist, when developed has a slightly obtuse edge profile. B) The obtuse profile, when sputter coated, creates a solid blanket layer of material which isolates the resist, impeding the liftoff process.

In this case, an image reversal process, described in the next section, would be better suited to the task.

4.1.2 Dark Field Mask Lithography Trials with Image Reversal

The next trials involved using an image reversal mask to create the photoresist masking strips in the desired regions. The mask used had a solid chrome layer which was only open (transparent) in the regions where the waveguides would be formed. This also required additional lithography steps to make the positive resist behave like a negative resist. The samples were spin-coated, baked, and exposed as before. Next the samples were given a reversal bake and high dose flood exposure. This changed the previously soluble sections of resist to polymerized ones, and the polymerized ones to soluble ones.

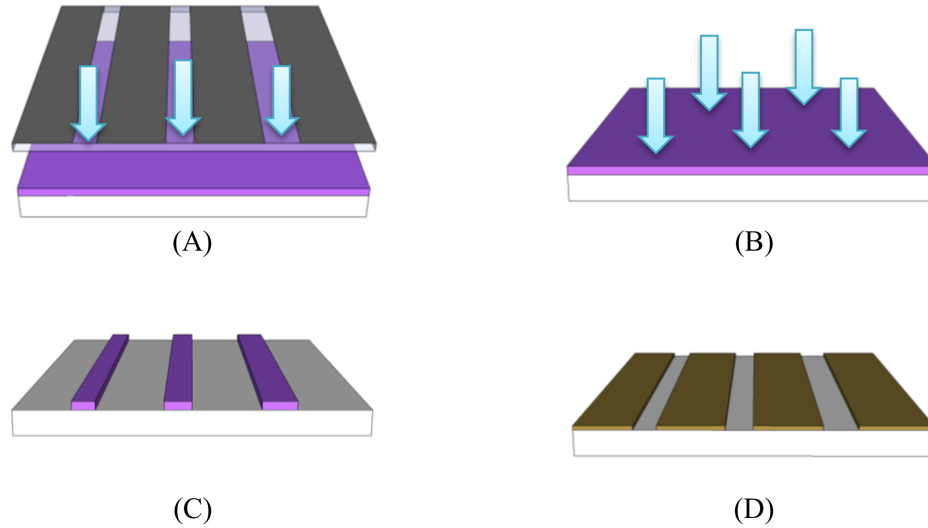

Figure 4.3. Dark field photolithography with image reversal steps. A) UV light exposure through photomask pattern makes the exposed photoresist more soluble in developer solution. B) Sample is baked and subjected to an unmasked flood exposure which reverses the image in the resist. C) Only the unmasked regions remain after development. Sample is sputtered and liftoff is performed. D) Remaining Ti layer is now the reverse image of the photomask.

After development strips of photoresist remained only in the waveguide locations as in the first trials. This time, though, the resist profile was inverted, being wider at the top than the bottom. The samples were titanium sputtered and then placed in acetone to dissolve the resist. The titanium proved stubborn to remove, even with subsequent ultra-sonication steps. The waveguide regions were only opened in limited regions of the sample. A heated photoresist-stripper solution was next used as a more aggressive means of resist removal, and samples remained in the solution for 24 hours. With much additional sonication the resist lifted off, but the excess sonication created many jagged edges along the waveguide contours.

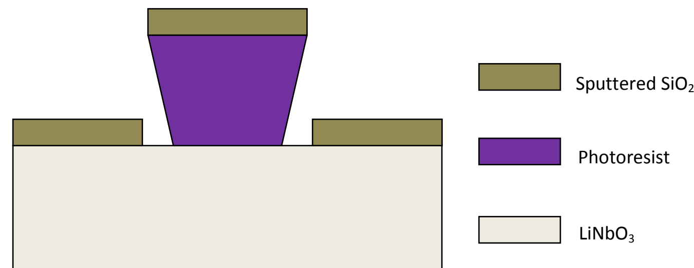

Figure 4.4. Resist sidewall profile after an image reversal exposure and development. This geometry is desired for lift-off lithography processes, where a sputtered film is deposited over the resist layer. The resist should be thicker than the film layer so that when the resist is removed in a liquid solution, the overlaying sputtered material is lifted off, while the rest of the substrate surface remains coated with the sputtered film.

It is assumed that the resist profile for these image-reversal samples was not as inwardly angled as anticipated causing complications in the liftoff process. It is also probable that the resist became hardened when subject to higher temperatures in the sputtering process, consequently making it more difficult to remove. Varying the resist thickness (by adjusting spin-coat speed or by adding a second layer prior to exposure) could create a taller resist profile which would facilitate the liftoff process. Exposing at a low exposure dose or raising the reversal bake temperature can also increase the degree of negativity in the resist profile [27].

4.1.3 Dark Field Mask Lithography Trials

Samples were also patterned directly on the protective masking layer using the image reversal mask from the Type II trials. Here some samples were sputtered with a 200nm titanium mask layer and others with a 200nm SiO_2 mask layer. Both of these depositions were performed in the newer AJA magnetron sputtering machine which has proven to offer much more uniform depositions than the EMMACO mag sputter system.

The samples were then cleaned and spin-coated with positive photoresist. The samples were aligned and exposed, making the resist covering the waveguide locations more soluble to the developing solution. After development the samples were etched in dilute hydrofluoric acid, which attacks titanium and silicon oxide. This effectively transfers the pattern developed in the resist to the protective masking layer. The resist was then removed leaving titanium or oxide

masked substrates that have channel openings where the waveguides were to be formed. An illustration of this process is featured below.

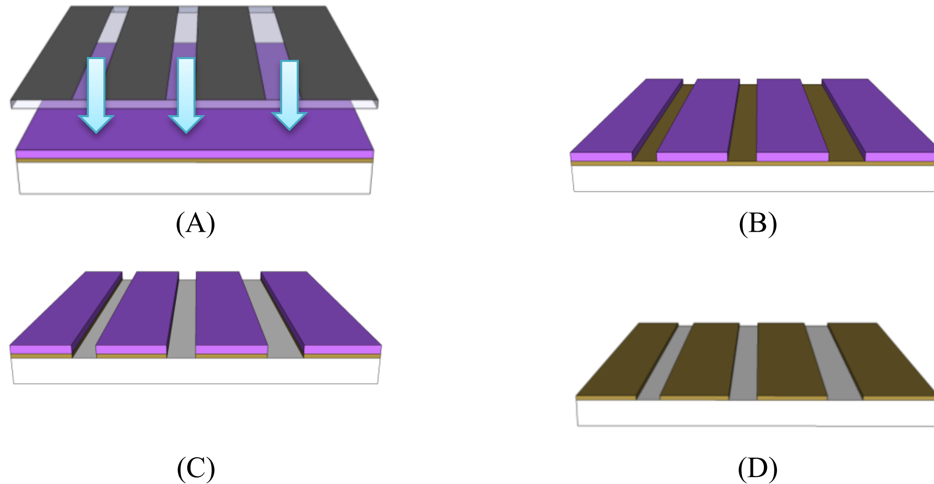

Figure 4.5. Dark field photolithography steps. A) Sample is sputtered with 200nm mask material, coated in resist, and exposed to UV light exposure through negative photomask pattern. B) Positive image is developed forming channels in the resist, resembling the photomask pattern. C) Masking layer is etched in HF solution until $LiNbO_3$ surface is exposed. D) Photoresist is stripped, leaving mask material (SiO_2 or Ti).

This mask type was a success, and led to production of the first working APE waveguides in our lab. Details can be seen in subsection 4.3.1. This method is much easier than the image reversal technique used in the Type II trials, and requires less process steps. This method is also has also been in use for the latest mask design and APE sample series C and D featured in section 4.3.

4.1.4 Image Reversal Lithography Trials

The ensuing trials used a resist image-reversal technique on a positive image mask. The goal is to deposit mask material on the sample surface and open up channels in the mask where it is desired that waveguides be formed. This is the same end result as the previous image reversal trials, but employs a clear-field mask that has not been image-reversed. The mask therefore is transparent with strips of chrome only in the regions where the waveguide channels will be defined.

This process begins by sputtering a 200nm mask layer on the sample surface. AJA sputtered SiO_2 was chosen due to its masking capability proven in the previous trials. The sample is cleaned, dehydrated, and spin-coated with photoresist. Next it is placed in the mask aligner for exposure. If the sample were developed at this stage it would leave resist strips in the waveguide locations. The sample is instead run through a reversal bake followed by a flood exposure to reverse the image in the photoresist.

The developed sample is protected by a layer of photoresist, with openings in the desired waveguide locations. The waveguide channels are then etched in this region and the samples are proton exchanged, annealed, polished, and measured as performed previously.

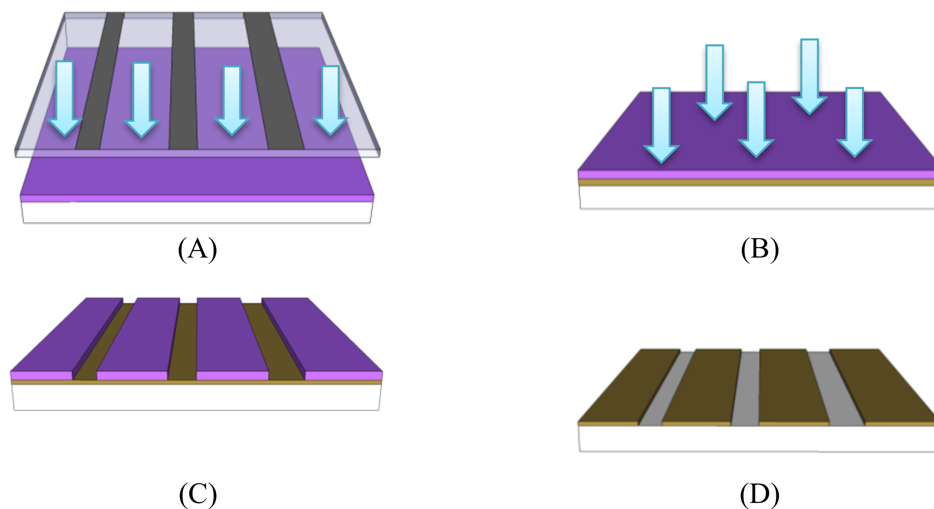

Figure 4.6. Image reversal photolithography steps. A) Sample is sputtered with 200nm mask material, coated in resist, and exposed to UV light exposure through positive photomask pattern. B) Sample is baked and subjected to an unmasked flood exposure which reverses the image in the resist. C) Reversed image is developed forming channels in the resist. D) Masking layer is etched in HF, and resist is stripped, leaving mask material (SiO2).

Developing a recipe for the lithography steps involved in the Type IV trials proved cumbersome. The same photoresist image-reversal recipe used in the Type II trials was initially employed, but there was difficulty getting the photoresist to develop properly. Samples were often underdeveloped, and immersing them in the developer solution for additional time had little to

no effect on improving image quality. Research and trial confirmed what was later found in literature [28], that too high a hotplate temperature for the reversal bake would thermally crosslink the resist, resulting in incomplete pattern develop.

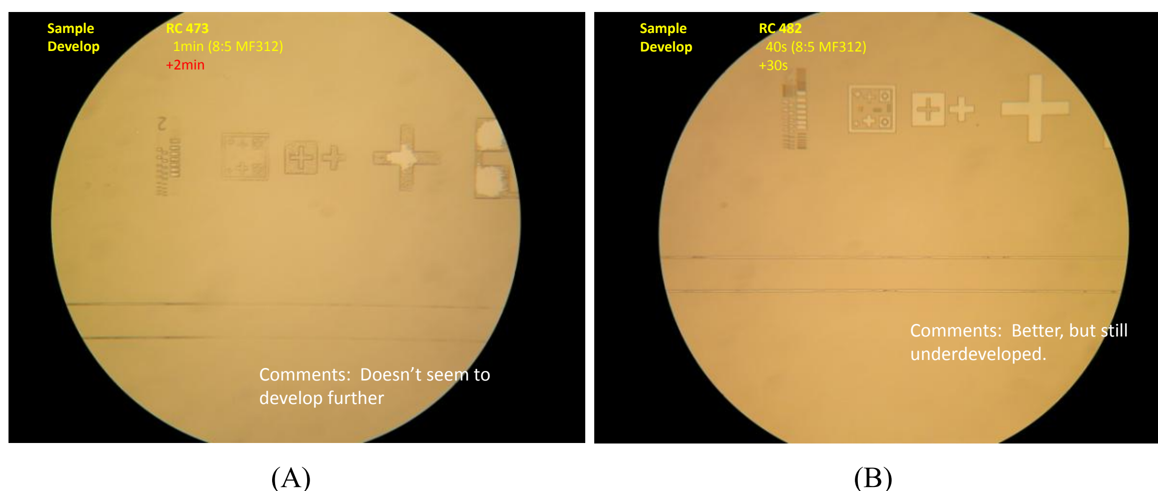

(A) (B)

Figure 4.7. Photoresist development images. A) Photograph of image reversal pattern during develop process. This pattern has not developed completely, as is evident by the rough patches around the alignment patterns which should be completely clear. B) Photograph of another sample with better develop than the previous. The large features of the alignment markers are completely developed, but the smaller ones, as well as the waveguide channels still have some stubborn resist that will not develop. The problem was found to be that the reverse bake temperature was too high and caused, inhibiting the development process.

Other factors that added to the difficulties were the obtaining of new photoresist, new UV bulbs, samples fracturing, and substrates that had particles under the mask layer, and flaking mask layer. The new photoresist was used to help improve the lithography process, but gave slightly different responses to UV light and develop times. After the recipe was adjusted a new UV bulb was installed in the aligner, with much stronger intensity than the previous bulb. The recipe was adjusted, but then that bulb was found to be faulty and another bulb was installed, which required further adjustments to the process. Sample cracking was thought to originate from the thermal stress caused by moving samples from the hotplate to a room temperature metal plate to cool, but it seems this is a standard process referred to as a chill plate by Mack [29], and the fractures were simply due to manufacturing defaults.

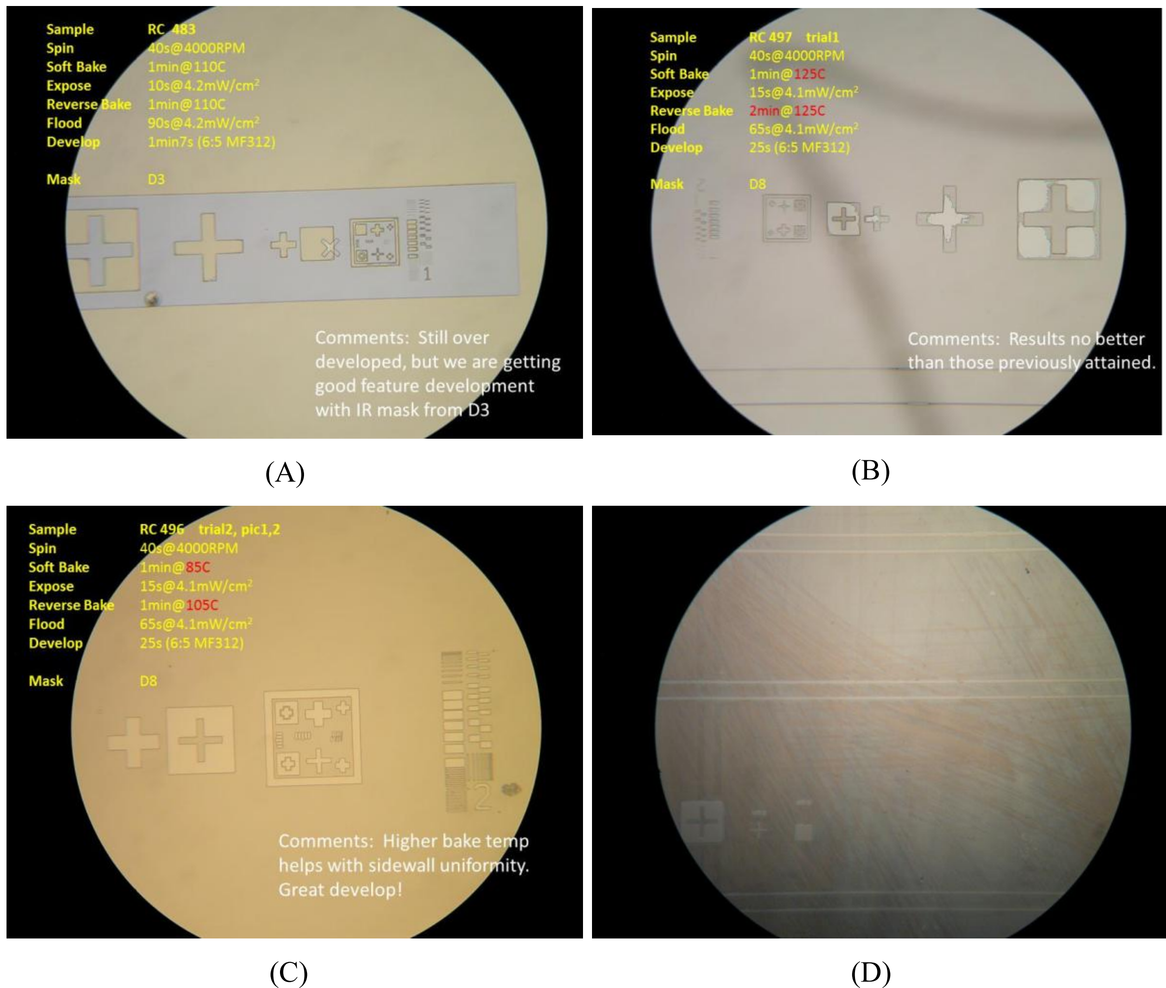

Figure 4.8. Photoresist development images. A) Photograph showing the tailoring of lithography recipe. This sample has problems with photoresist adhesion, which are overcome by raising the hot plate temperature for soft bake. B) This sample shows an incomplete develop, which was found to be due to too high a reversal bake temperature. C) Photograph of an ideal development. Alignment markers have square corners and have are completely clear in intended regions. D) This sample had many scratches on the layer, thought to be caused by abrasive rub with cotton swab during cleaning. Problem was actually due to variation in SiO_2 deposition process and was corrected.

4.2 ETCHING AND SURFACE ROUGHNESS

This section reports on the surface smoothness measured after removing the mask material from proton exchange samples. Images were taken using a Nikin Coolpix 4500 camera attached to a Lyca microscope. Surface profile measurements were performed using a Dektak profilometer.

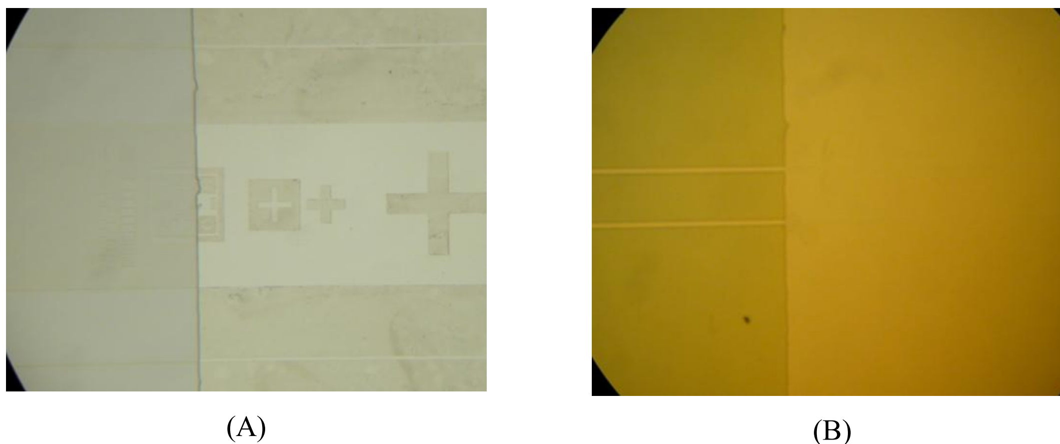

(A) (B)

Figure 4.9. SiO_2 protective mask removal. A) Photograph from inspection of SiO_2 mask removal on APE sample RC 482. The image is centered on a photolithography alignment marker, used for adding subsequent photolithographic layers. It was also a reference point used in the surface profiling measurements. The left-half of the image is protected by a photo resist layer, while the right-half is exposed. This sample has been etched for 30 seconds in dilute HF, and is under-etched as is evident by material still visible on the right half of the image. B) Photograph from SiO_2 mask removal after 1 minute wet etch in HF, taken using a special light filter. The photoresist layer has also been removed. Image is centered on two waveguides and shows the contrast between the masked (left) and unmasked (right) portions.

The samples used in these experiments had been exchanged, annealed, and measured for propagation loss. They were then re-coated with photoresist and patterned so that only the center portion of the waveguide sample would have the masking layer removed. The profile measurements use two locations for reference: lithography alignment marker and two waveguides with location chosen at random. The photographs above show the masked and unmasked regions for a partially etched sample (Figure 4.9-A) and completely etched sample (Figure 4.9-B).

The alignment marker location was chosen since it features a large section of bare lithium niobate, as well as SiO_2. This should show an observable depth transition should there be any

SiO_2 remaining on the surface. The waveguide location was chosen for measurement since it is desired to fabricate a secondary layer in this region with a ring resonator, with smooth surfaces expected to increase optical coupling.

The following measurements were performed using the Dektak surface profilometer. This device is computer controlled and drags a stylus over the region of interest at a user specified rate and length. Any changes in surface uniformity cause vertical travel in the stylus, which is transduced to an electrical signal similar in a fashion similar to that of a stylus used in vinyl record playback. A camera with magnification lens is used to align the sample in the region of interest, and the stylus is then scanned across the stationary sample surface. A computer readout shows the variation in surface height with angstrom level resolution.

Table 4-1. Surface profile readings for three SiO2 masked samples. The mask region was removed by wet etch in dilute HF.

Surface Uniformity

Sample	align marker	over 3 WGs
RC 482	+- 40A°	+-60A°
RC 483	-	+-70A°
RC 493	+-35A°	+-60A°

These measurements show an average surface roughness of +-60 angstroms in the waveguide region. This is a significant improvement in comparison to our Ti diffused waveguide process which produces a surface bump exceeding 100nm in the waveguide region, and with 20nm of non-uniformity [30]. By comparison there is no bump present on the APE waveguide surface, with non-uniformity spanning 12nm.

When coupling light from a waveguide to a chalcogenide ring resonator, surface roughness adversely affects the coupling capacity of the system [30]. It is anticipated that the smooth surface offered by the APE fabrication process will lead to the fabrication of ring resonators with lower waveguide to ring coupling losses.

4.3 WAVEGUIDE TRANSMISSION MEASUREMENTS

All APE samples are measured using the LUNA Optical Vector Analyzer, which scans a broad spectrum of 1525 to 1610nm. Each sample has multiple waveguides patterned on it. These devices are placed on a translation stage with coupling fibers at each end. Index matching gel is used to assist in the transition from silica fiber (n= 1.45) to $H:LiNbO_3$ waveguide (n= 2.3). The fibers are aligned under microscope until they line up with the waveguide, and then the optical source is scanned to characterize the device for optical transmission across the spectrum.

4.3.1 Initial Trials

Initial APE samples were exchanged and annealed following the Suckoski and Leonburger process [3], with a 30 minute exchange at 200°C, and 4 hour anneal at 350°C. This recipe aims to produce low loss single-mode waveguides for operation at 1550nm.

For the first samples, the masking layer was removed from the samples prior to anneal. The resulting surface was completely uniform to the naked eye, and only upon close inspection under microscope with special optics could one see the exchanged waveguide regions. This made it impossible to butt-couple fibers to the waveguides for our measurement setup.

Subsequent samples did not have the masking layer removed prior to annealing, so that the waveguides channels would be visible on the masking layer for measurement purposes. These samples were then polished and measured on the LUNA optical vector measurement system. The SiO_2 masked samples were the only ones to exhibit light transmission, which showed as TE only as anticipated. The samples were lossy and also showed some multi-mode or wavelength dependent behavior. An example measurement is shown in Figure 4.10.

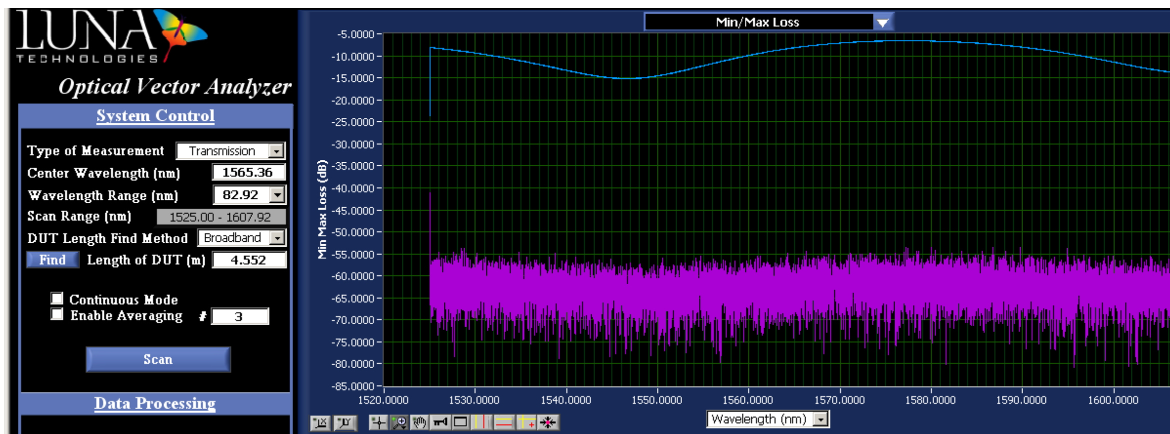

Figure 4.10. Measurement from 2cm length sample RC 416, featuring a 200nm SiO_2 mask, and fabricated by 30 minute exchange at 200°C, followed by a 4 hour anneal at 350°C. The blue line represents the TE mode, and the magenta line the TM mode. The separation seen is characteristic to APE waveguides fabricated on x-cut crystals, transmitting only the TE mode. This sample shows strong wavelength dependence on transmission, with a loss of 5dB at best after accounting for fiber to fiber loss. This translates to a loss of 2.5dB/cm at 1575nm, and 7.5dB/cm at 1545nm.

This was the first breakthrough in creating proton exchanged waveguides at Texas A&M University. Center portions of the masking layer were removed and no waveguides were visible, just as when the mask was removed prior to annealing. The waveguide regions were still visible under special optics, and more importantly Dektak surface profile measurements showed a uniformity of +-80A. This is much smoother than the bump left on the surface of Ti-diffused waveguides and will hopefully enhance coupling into successive waveguide or ring-resonator layers.

The titanium masked samples did not transmit light. It is suspected that the titanium surrounding the waveguide channel could be absorbing the incident light. Upon further inspection some of the waveguides on the Ti-masked samples had not been sufficiently polished, which may have also contributed to transmission failure.

4.3.2 Series A (RC 521,522)

This series of waveguides was fabricated using mask D8, a lithography mask featuring 7um width waveguides intended for Ti diffused waveguide patterning. The samples were patterned using the image reversal lithography technique mentioned in subsection 4.1.4 and etched via RIE. The samples were then immersed in pure benzoic acid for 20 and 25minuties (521, 522 respectively). Afterward they were annealed at 350°C in a series of time intervals, with measurements preformed between anneals.

The furnace temperature varied between 350 and 370°C during these runs. These samples were fabricated in effort to follow recipes by Suchoski and Leonburger, and Il'ichev for use with telecom wavelengths [3], [4]. When previous samples were fabricated using similar processes (4 hour anneal), they would have high loss. One can only assume that this is due to the diffusion rate of our acid or equipment being different from the literature. These samples were fabricated before any of the simulation programs had been written, and were based upon trial and error. Alpha phase maps have now been created to span this temperature fluctuation, and the resultant plots show that the waveguides have not had sufficient anneal time to reach alpha phase if calculations are performed using Almeida's diffusion constants.

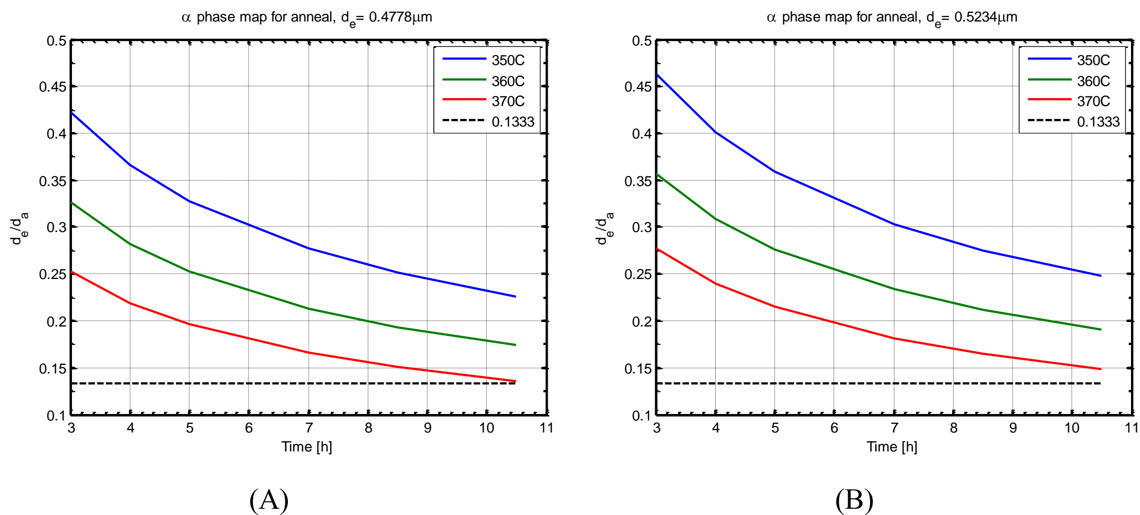

(A) (B)

Figure 4.11. A) This plot simulates the annealing of a PE sample fabricated by immersion in benzoic acid for 20 minutes at 200°C (d_e= 0.4478 μm). The plot shows the d_e/d_a relation for a series of simulated anneals spanning 350-370°C, the approximate temperature fluctuation of the anneal furnace for this experiment. Samples should reach the low loss α phase when their d_e/d_a drops below the 0.133 reference line. B) These plots are similar to those in (A), but feature an exchange time of 25minutes at 200°C (d_e= 0.5234μm). Given the longer initial exchange time, these samples should take longer to reach alpha phase.

According to these simulations the waveguides would only have reached α phase if the temperature was well in excess of the 350°C. The thermocouple used to measure the furnace temperature averaged 358°C for the majority of the runs. The measurement data from these guides is given in the following table.

Table 4-2. RC 521, 360°C anneal.

Measurements from 25min exchange @ 200°C			
Anneal Time(h)	Insertion Loss (dB)	d_a [μm]*	d_e/d_a*
3	15	1.466	0.325
4	13	1.693	0.282
5	1	1.893	0.252
7	10	2.240	0.213
.5	12	2.469	0.193
10.5	2	2.744	0.174

**Simulation Value*

Table 4-3. RC 522, 360°C anneal.

Measurements from 30min exchange @ 200°C			
Anneal Time(h)	Insertion Loss (dB)	d_a [μm]*	d_e/d_a*
3	14	1.46	0.356
4	15	1.693	0.30
5	15	1.893	0.276
7	16	2.240	0.233
8.5	14	2.469	0.211
10.5	3	2.74	0.190

**Simulation Value*

These waveguides were the first from those fabricated in our lab to reach low propagation loss. Each successive anneal increased the anneal depth d_a, bringing the samples closer to the low loss crystal α phase. These samples follow a trend similar to those observed by Howerton during his anneal series, where increasing the d_a lowered propagation losses, with the lowest loss being when the samples reach α phase [10]. It can be concluded that since 10.5 hours was sufficient for these samples to reach a state of low-loss, that the Almeida diffusion coefficients do not accurately describe the diffusion rates experienced in these trials.

4.3.3 Series B, (RC 523,525)

This second series was run to see how exchanging to a shallower depth, with anneal time comparable to those samples fabricated in Series A. These samples were measured only 3 times during the anneal process, compared to 6 times with the Series A experiments. The samples were found to reach the low loss regime quicker than those fabricated in Series A, due to the

shorter initial exchange period forming a smaller d_e and thus reducing the anneal depth d_a requirements to reach alpha phase.

Table 4-4. RC 523, 360°C anneal.

Measurements from 15min exchange @ 200°C			
Anneal Time(h)	Insertion Loss (dB)	d_a [µm]*	d_e/d_a*
4	35	1.693	0.218
5.5	7.5	1.986	0.18
9	4	2.540	0.14

**Simulation Value*

Table 4-5. RC 525, 360°C anneal.

Measurements from 20min exchange @ 200°C			
Anneal Time(h)	Insertion Loss (dB)	d_a [µm]*	d_e/d_a*
	16.5	1.693	0.252
5.5	9	1.986	0.215
9	3.5	2.54	0.168

**Simulation Value*

Despite measurements showing that these waveguides had reached the low-loss regime, the simulated anneal depth d_a and d_e/d_a ratios performed using Almeida's diffusion constants (see subsections 2.3.1 and 2.3.5) predicts that these samples had not been annealed long enough to reach alpha phase.

A comparison simulation was made to plot Almeida's diffusion constants versus those published by Howerton. The simulation below shows anneal parameters for creating alpha phase waveguides, with initial exchange of either 15 or 25 minutes in pure benzoic acid heated to 200°C. The simulation subjects these samples to thermal anneal at 360°C, and follows them for a timespan of 24hours. The simulated d_e/d_a ratio is plotted against time for each sample in this simulation series featured in Figure 4.12.

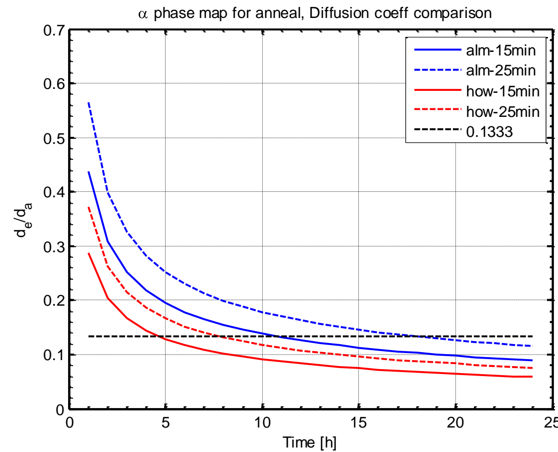

Figure 4.12. Series of anneal simulations created to compare times required to reach alpha phase (d_e/d_a<0.133). The simulation follows two samples exchanged for 15 and 25 minutes, and simulates diffusion for each using both Almeida and Howerton's respective diffusion constants.

This model shows that Howerton and Almeida reported significantly different diffusion rates. Our experimental results for samples exchanged for 15 and 25 minutes fall roughly between the two simulated diffusion rates. An average of these two values could be used for further simulation, but actual diffusion measurements for the exchange and anneal steps would certainly provide a more accurate model.

4.3.4 Series C (RC 548, 569)

With a rough idea of diffusion times in mind, another series of samples was fabricated using a new mask (D9) designed specifically for positive photolithography patterning of APE samples. This mask did away with many of the difficulties encountered with image reversal lithography that were described in subsection 4.1.4. A second pattern was also included on this mask to facilitate removal of the SiO_2 masking layer after anneal.

These samples were fabricated using an exchange time of 22 minutes, at a temperature of 200°C. They were annealed and measured in steps as before, and showed similar trends to those samples previously reported. The measurements are included in the tables below. The SiO_2 mask layer was removed from sample 569, and post removal measurements showed no change in propagation loss.

Table 4-6. RC 548, 360°C anneal.

Measurements from 22min exchange @ 200°C			
Anneal Time(h)	Insertion Loss (dB)	d_a [μm]*	d_e/d_a*
4	32	1.6937	0.2651
7.5	7.5	2.3193	0.1936
10 5	3	2.7442	0.1636

Simulation Value

Table 4-7. RC 569, 360°C anneal.

Measurements from 22min exchange @ 200°C			
Anneal Time(h)	Insertion Loss (dB)	d_a [μm]*	d_e/d_a*
4	-	1.6937	0.2651
7.5	10	2.3193	0.1936
10.5	3.75	2.7442	0.1636

Simulation Value

Sample 569 has been sputtered with a 0.431um layer of As_2S_3 and at the time of this writing is being sent to Penn State University for ring resonator patterning. It is anticipated that a ring resonator with this thickness of chalcogenide glass will allow a TE operation ring resonator, a first for our group. It is also hoped that the smooth surface of the APE waveguide will improve waveguide to ring coupling.

4.3.5 Series D (RC 529, 542, 549, 559)

Another series of samples was fabricated using the new mask, and with plans to lower fabrication time by increasing the anneal temperature from 360°C to 400°C. This should reduce the required anneal time to 1hour 30minutes for samples that have been exchanged for 15 and 20 minutes. Samples exchanged for 25 minutes should require a 2hour anneal to reach alpha phase.

Table 4-8. Calculated values: d_e- initial exchange depth, d_a anneal depth. Low loss guides formed when d_e/d_a <= 0.133.

Sample	Exchange Temp	Time	d_e (μm)	Anneal Temp	Time	d_a (um)	d_e/d_a
RC 529	200C	15min	0.556	400C	1h30min	5.171	0.108
RC 542	200C	20min	0.642	400C	1h30min	5.171	0.124
RC 549	200C	20min	0.642	400C	2h	5.971	0.108
RC 559	200C	25min	0.717	400C	2h	5.971	0.120

These samples have been through one anneal step, allowing 30 extra minutes for the sample to reach the desired temperature in a pre-heated furnace. At the end of the anneal period, the furnace was reading 391°C, which is lower than anticipated. This small change in temperature greatly affects the anneal depth d_a as is shown in the following simulation plot.

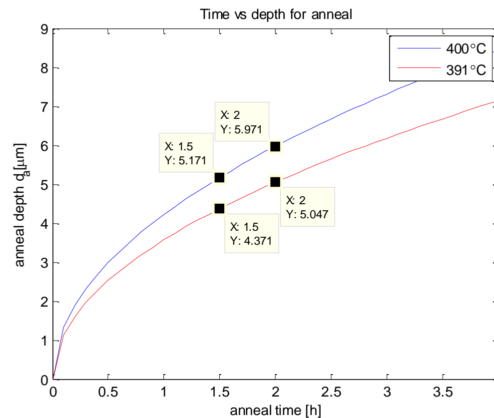

Figure 4.13. Simulation plot showing the large influence temperature change has on anneal depth and time. This stresses the importance of proper furnace calibration for accurate and reproducible APE waveguide fabrication

This samples will require more time to reach the desired anneal depth and alpha state. According to this plot the samples should require an extra 1.5 hours to reach the desired anneal depth.

4.4 MODE PROFILE MEASUREMENTS

Samples RC 521 and 548 were measured using TE polarized light centered at 1550nm. They were fabricated using the following conditions:

-**RC 521**, patterned using mask D8 (image reversal)
x-cut LN, PE 25min@200°C, anneal 10.5h@350°C

-**RC 548**, patterned using mask D9 (positive lithography)
x-cut LN, PE 22min@200°C, anneal 10.5h@360~370°C *
**the furnace temperature fluctuated a bit from start to finish*

For determining the resolution of the profiler, I measured two waveguides on sample 521 that are 195um apart. The position of the focusing lens was kept constant and data was taken for both waveguides by moving the incoming fiber only. I then determined the separation between the center beam x location in the data for both waveguides, which was 5490 pixels, or arbitrary units. The resolution for those measurements was therefore 195um/5490pix. The profiler setup

used a 1550nm laser, and Corning lists their SMF-28 fiber as having a 10.7um MFD at this wavelength.

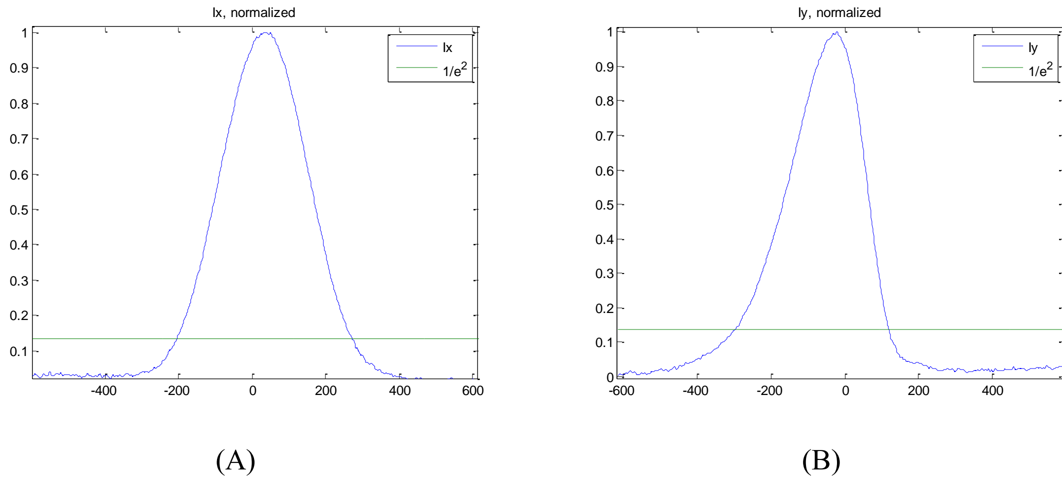

(A) (B)

Figure 4.14. Intensity profile data from ThorLabs Beam Profiler, plotted in MATLAB. A) Intensity profile in x-direction, symmetric. B) Intensity profile in y-direction, asymmetric.

Intensity profile scans in the x and y directions were saved for each waveguide measured. Scans were later plotted and analyzed in Matlab. The code will find the peak location as well as the two $1/e^2$ crossing points for the intensity profile, needed to calculate the beam width. This is equivalent to the 1/e crossing points for the E field profile. These crossing points are also needed in order to determine $\sigma_1, \sigma_2, \sigma_3$ for solving the fiber to waveguide mode mismatch equation (see figure 3). For the x direction (symmetric), σ_3 is calculated as half the $1/e^2$ width. For the y-direction (asymmetric), one must find the distance from the center peak to the $1/e^2$ crossing points in order to calculate σ_1, and σ_2. The solution to these calculations is in arbitrary units used by the beam profiler. This must then be converted to um by the aforementioned conversion factor: 195um/5490pix.

The mismatch factor η, was calculated using equation 17, as well as coupling loss for each measurement.

The following table was created using the measurement data from samples RC 521 and 548. It includes the calculated beam widths in the x and y directions, as well as the mode mismatch factor and fiber coupling loss.

Table 4-9. Measurement data from beam profile measurements.

Measurement Data							
Sample	**$1/e^2$(Ix) (um)**	**$1/e^2$(Iy) (um)**	σ_1 **(um)**	σ_2 **(um)**	σ_3 **(um)**	η **(um)**	**Coupling loss (dB)**
RC521_stwg8	13.14	11.12	6.71	4.41	6.57	0.947	0.236
RC521_stwg9	11.90	9.49	5.22	4.28	5.95	0.98	0.087
RC548_wg10	16.91	14.87	9.7896	5.0872	8.4574	0.798	0.983
RC548_wg11	16.79	15.78	9.918	5.857	8.394	0.805	0.941

The MFD of sample 521 is very close to that of the fiber. Sample 548 has a larger MFD, likely due to the higher than anticipated anneal temperature causing a larger than desired anneal profile. With this larger profile comes greater fiber mismatch loss.

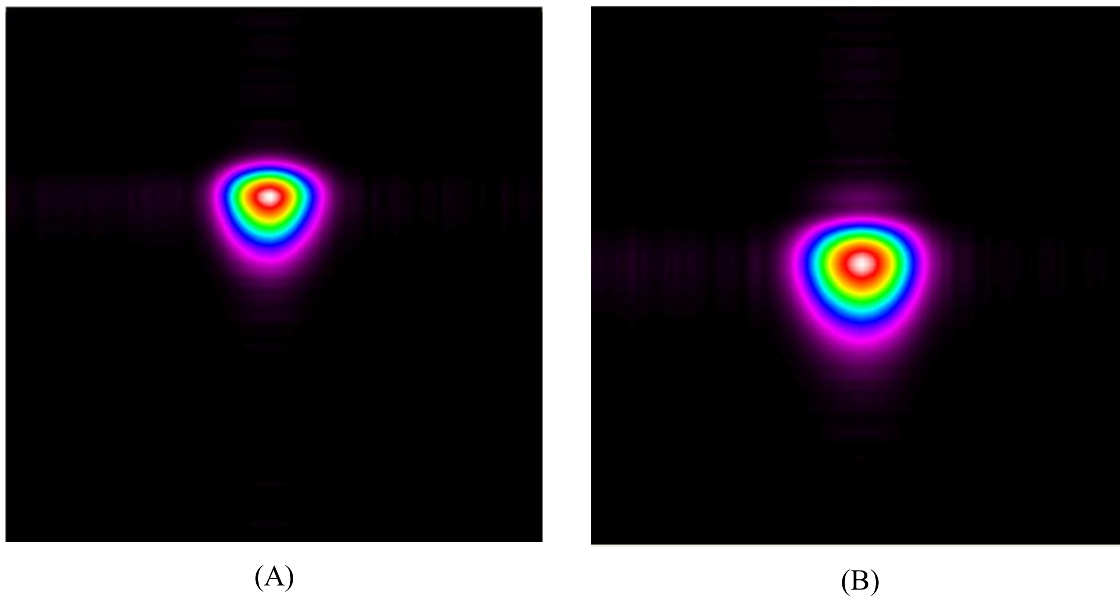

(A) (B)

Figure 4.15. Beam profiler screen captures. A) RC 521, waveguide 8. B) RC 548, waveguide 10.

The beam profile images show single mode propagation at 1550nm. The profile projection shapes match that of the FimmWave simulations. See following image for an example.

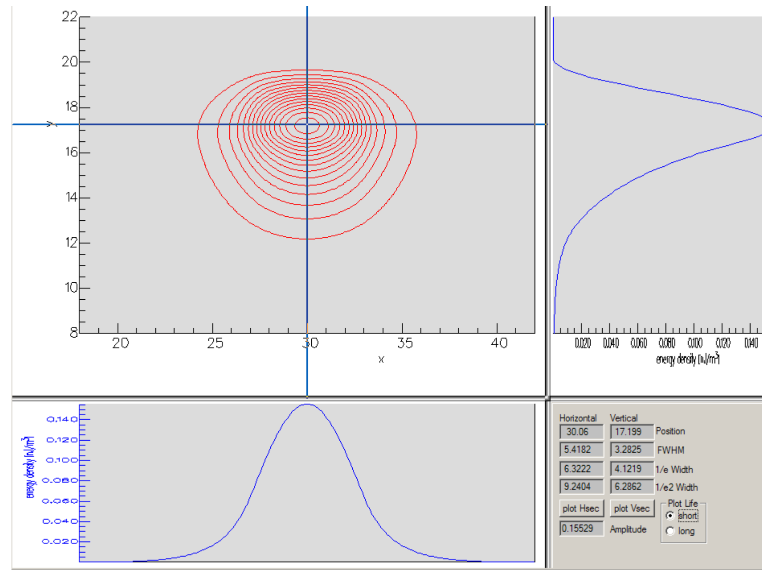

Figure 4.16. FimmWave APE waveguide simulation, intensity profile

5. CONCLUSION AND FUTURE DIRECTION

Annealed Proton Exchange waveguide fabrication has just begun for the Photonics group at Texas A&M. Working devices have been proven, beginning by simply following recipes found in literature. APE waveguides have been fabricated which exhibit low propagation loss, and feature a smooth surface favoring vertical device integration. There are a number of ways that this process can be improved, which could eventually lead to its use, alongside or in place of our current titanium diffused waveguide process, in creating ring resonators and phase modulators. The following sections offer suggestions for methods to improve the current proton exchange fabrication process.

5.1 MORE ROBUST EXCHANGE APPARATUS

The current PE setup employs a simple insulated beaker heated by convection and mixed by magnetic stirrer. The weakness in the setup is the variation in acid temperature occurring namely when samples are introduced into the melt and heated. Current PE times begin when the melt has reached proper temperature, but sometimes exceed this temperature before settling down to the desired reaction temperature. This higher temperature certainly diffused hydrogen to a greater depth than desired, and as has been seen will increase diffusion time requirements.

A proposed solution would employ an exchange setup similar to that described by Almeida with a heated silicone oil bath surrounding the benzoic acid melt [9]. A separate empty vessel would also be placed in the bath and used to warm samples on deck , waiting to be exchanged, to approximately the reaction temperature prior to immersion in the acid. The oil bath would be insulated with a larger version of silica fiber filled fiberglass insulator sleeve currently in use. The lid should be constructed of PTFE, with two holes; one for the exchange beaker, and another for warming the sample. A PTFE sample holder should be fabricated to facilitate moving samples from the warm-up beaker to the exchange beaker. Finally, two PTFE covers should be fabricated to prevent thermal loss from the sample openings, and allow insertion of thermocouple probe for temperature monitoring.

This setup should raise the heat capacity of the setup and provide a much more stable temperature than that of our current setup, increasing repeatability of experiments and predictability with computer simulations. It would also reduce thermal shock for samples with

respect to the current process, though this may not be a problem for x-cut samples [2]. It could also be built large enough to accommodate fabrication of longer samples.

5.2 BETTER ANNEAL FURNACE CHARACTERIZATION AND CALIBRATION

Due to the temperature sensitivity of the APE diffusion process, small variations of anneal temperature can greatly impact the fabrication process. This has been outlined in subsection 2.3.2, and demonstrated in 4.3.5. The current furnace system has no end-cap, and addition of a cap with accommodation for thermocouple probe would increase repeatability of temperature measurements with relation to the current system which requires moving the probe around manually until it looks like it's in the right spot.

The furnace should also be calibrated for a region spanning from the center, where samples are placed, to ensure that multiple samples placed in the furnace at once will experience the same anneal temperature. The temperature should be monitored on a regular basis to ensure correct diffusion times and temperatures. There is already a LabVIEW program setup to monitor furnace temperature with time. Using this system would also give insight into temperature fluctuations during the anneal period.

Having a more consistent furnace temperature should allow repeatable fabrication of APE samples, and enable increasing the furnace temperature to 400°C for remaining fabrication thereby reducing anneal times.

5.3 CHARACTERIZATION OF BENZOIC ACID DIFFUSIVITY FOR SYSTEM

Once a more robust system of exchange and anneal are in place, the diffusivity for these processes should be characterized. Other reports have used SIMS or X-ray diffraction to determine hydrogen concentration as a function of sample depth.

Samples should be proton exchanged at either a constant temperature and for different times, or at different temperatures for the same amount of time. The proton diffusion rate can then be accurately determined by solving the Arrhenius relation for these samples, or by determine the activation energy and diffusivity for these samples. I would suggest fabricating samples at 200°C for 10, 20, and 30 minutes and use these to determine the diffusion coefficient at 200°C, since other temperatures do not seem necessary if following the current design process.

Once the proton exchange diffusion rate is known, the anneal diffusion rate should be characterized. It would then be beneficial to anneal a series of samples fabricated using identical PE processes, ie same exchange depth d_e, and then anneal them for the same amount of time but at different temperatures. For example one could exchange samples for 20 minutes at 200°C, and then anneal one at 350°C for 4 hours, another at 375°C for 4 hours, and the third for 4hours at 400°C.

Knowing the actual diffusion coefficients from our experimental setup would allow us to have much more control over APE design for future device fabrication.

5.4 WAVEGUIDE MODE PROFILE MEASUREMENT AND OPTIMIZATION

As shown in Figure 2.17, though a waveguide may have attained sufficient anneal diffusion depth d_a to be in the low-loss α crystal phase, it the mode profile can have significant deviation from that of the MFD of the coupling fibers used for device integration. This introduces substantial loss in the system, but can be seen as a low-hanging fruit means of improving device performance and quality.

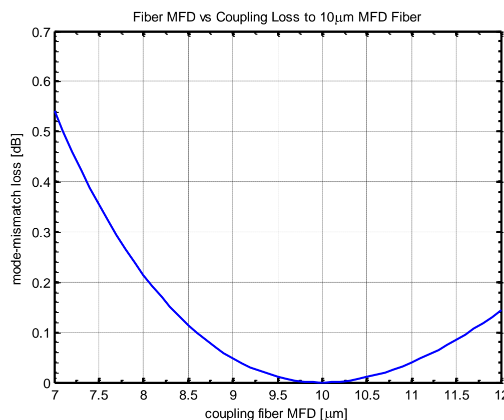

Figure 5.1. Simulation of mode-mismatch in fiber to fiber coupling. The optimal fiber is taken to be 10μm, and the variable fiber is shown to span diameters from 7 to 12 μm. Fiber diameter is plotted verses mode-mismatch loss to show that a fiber of the same diameter would theoretically incur zero mode-mismatch loss, while notable losses are incurred as mode side deviates from that of the reference fiber.

The above chart simulated mode-mismatch loss in fiber to fiber coupling as one fiber mode size differs from another. It is important to note that the simulations were run for a fiber with

symmetric Gaussian profile, and that APE waveguides would likely experience greater loss due to their asymmetric MFD. For comparison the waveguide simulated in section had a MFD of 7.6μm, and a mode mismatch loss of 0.7dB, whereas according to this chart a fiber with 7.6μm MFD would only experience a 0.35dB mode-mismatch loss. In a waveguide integration or measurement setup, this loss would be present at each end of the device. Matching the MFD of the waveguide to the fiber would therefore have the potential to greatly improve the loss of the system. One could alternatively aim to match the MFD of Ti diffused waveguides currently in use in the Photonics lab to enhance the interchangeability of processes.

The waveguide MFD can be determined with a beam profiler. For an empirical means of matching the fiber MFD a sample should be annealed in incremental steps, with beam profile measurements between each step. A sweet spot can then be found for fabricating waveguides with an MFD close to that of the fiber. The previously mentioned fabrication improvements would go towards improving the repeatability of the optimized MFD, as well as enabling computer simulation of parameters suitable for multiple fabrication temperatures. Higher anneal temperatures could be used to reduce device fabrication time, while lower temperatures could be used to have greater control over MFD.

5.5 DEVICE INTEGRATION

Using the APE waveguide as a building block, devices that have been proven to function with our existing titanium diffused waveguide process could be applied to APE waveguides. Ring resonators, disc resonators, and glass microspheres could be used to test optical coupling into from APE waveguides. Mach-Zender interferometers could be fabricated including electrodes for testing proper state of the crystal phase and electrooptic coefficient in APE waveguides. Small bends with minimal loss could be integrated into existing designs by inclusion of exchange-only PE waveguides with inherently large Δn.

5.6 MODE DISPERSION ANALYSIS

More information about mode propagation and cutoff could be determined using the prism coupling method. In order to obtain maximum benefit, a relatively deep APE waveguide should be fabricated which will allow multiple modes to propagate at 633nm. From these measurements one can determine the mode cutoff for each mode and extrapolate this to 1530nm light using the IWKB method. We currently do not have such a setup in our lab, and so this procedure would need to be outsourced to a commercial measurement facility.

5.7 DETAILED SURFACE INSPECTION

The final suggested step to further APE work is to use high resolution imagery to inspect the surface. The surface measurements performed using a surface profiler approach the detection limits of this apparatus. AFM or other means could be used to verify surface profilometer readings and ensure waveguide smoothness. This is the appendix

REFERENCES

[1] J. L. Jackel, "Proton exchange: past, present, future," *SPIE Vol. 1583 Integrated Optical Circuits*, pp. 54-63, 1991.

[2] J. L. Jackel, C. E. Rice, and J. J. Veselka, "Proton exchange for high-index waveguides in LiNbO3," *Applied Physics Letters*, vol. 41, no. 7, pp. 607-608, 1982.

[3] P. G. Suchoski, T. K. Findakly, and F. J. Leonberger, "Stable low-loss proton-exchanged LiNbO3 waveguide devices with no electro-optic degradation," *Optics Letters*, vol. 13, no. 11, pp. 1050-1052, 1988.

[4] I. V. Il'ichev, A. S. Kozlov, P. V. Gaenko, and A. V. Shamrai, "Optimisation of the proton-exchange technology for fabricating channel waveguides in lithium niobate crystals," *Quantum Electronics*, vol. 39, no. 1, pp. 98-104, 2009.

[5] A. Yi-Yan, "Index instabilities in proton-exchanged LiNbO3 waveguides," *Applied Physics Letters*, vol. 42, no. 8, pp. 633-635, 1983.

[6] R. V. Roussev, "Optical-Frequency Mixers in Periodically Poled Lithium Niobare: Materials, Modeling, and Characterization, a Thesis," PhD Thesis, Stanford University, 2006.

[7] X. Xie, et al., "Picojoule threshold, picosecond optical parametrc generation in reverse proton-exchanged lithium niobate waveguides," *Journal of The Optical Society of America B*, vol. 21, no. 7, pp. 1397-1402, 2004.

[8] Y. N. Korkishko, V. A. Fedorov, O. Y. Feoktistova, and T. V. Morozova, "Effect of SiO2 cladding on properties of annealed proton-exchanged LiNbO3 waveguides," *Journal of Applied Physics*, vol. 87, no. 9, pp. 4404-4409, 2000.

[9] J. M. M. M. d. Almeida, "Design methodology of annealed H+ waveguides in ferroelectric LiNbO3," *Optical Engineering*, vol. 46, no. 6, pp. 064601-1-064601-13, June 2007.

[10] M. M. Howerton, W. K. Burns, P. R. Skeath, and A. S. Greenblatt, "Dependence of Refractive Index on Hydrogen Concentration in Proton Exchanged LiNbO3," *IEEE Journal of Quantum Electronics*, vol. 27, no. 3, pp. 593-601, 1991.

[11] A. Passaro, M. A. R. Franco, N. M. Abe, and F. Sircilli, "The Effect of the Proton-Concentration-to-Refractive-Index Models on the Propagation Properties of APE Waveguides," *Journal of Lightwave Technology*, vol. 20, no. 8, pp. 1573-1577, 2002.

[12] Y. N. Korkishko and V. A. Federov, "Relationship between refractive indices and hydrogen concentration in proton exchanged LiNbO 3 waveguides," *Journal of Applied Physics*, vol. 82, no. 3, pp. 1010-1017, 1997.

[13] P. Ganguly, "A semi-analytic technique to determine the propagation constant of periodically segmented Ti:LiNbO3 waveguide," *Advances in Applied Science Research*, vol. 2, no. 1, pp. 136-144, 2011.

[14] Corning. (2011) Corning SMF-28 ULL Optical Fiber With Corning Ultra-Low Loss Technology. [Online]. http://www.corning.com/WorkArea/showcontent.aspx?id=14357

[15] L. McCaughan and E. J. Murphy, "Influence of Temperature and Initial Titanium Dimensions on Fiber-Ti:LiNbO3 Waveguide Insertion Loss at lambda= 1.3um," *Journal of Quantum Electronics*, vol. 19, no. 2, p. 1310136, 1983.

[16] J. Rams and J. M. Cabrera, "Preparation of proton-exchange LiNbO3 waveguides in benzoic acid vapor," *Journal of The Optical Society of America B*, vol. 16, no. 3, pp. 401-406, 1999.

[17] J. L. Jackel, "Reverse Exchange Method for Burying Proton Exchanged Waveguides," *Electronic Letters*, vol. 27, no. 15, pp. 1360-1361, 1991.

[18] Y. N. Korkishko, V. A. Fedorov, and T. M. Morozova, "Reverse Proton Exchange for

Buried Waveguides in LiNbO3," *Journal of The Optical Society of America A*, vol. 15, no. 7, pp. 1838-1842, 1998.

[19] D. J. Bamford, D. J. Cook, S. J. Sharpe, and A. D. Van Pelt, "Widely tunable rapid-scanning mid-infrared laser spectrometer for industrial gas process stream analysis," *Applied Optics*, vol. 46, no. 19, pp. 3958-3968, 2007.

[20] E. Y. B. Pun, S. A. Zhao, K. K. Loi, and P. S. Chung, "Proton-Exchanged LiNbO3 Optical Waveguides Using Stearic Acid," *IEEE Transactions Photonics Technology Letters*, vol. 3, no. 11, pp. 1006-1008, 1991.

[21] Y. N. Korkishko, et al., "Nonlinear optical properties of different types of proton exchanged LiNbO3 and LiTaO3 waveguides," *Proceedings of SPIE Vol. 4944*, vol. 4944, pp. 268-279, 2003.

[22] K. El Hadi, et al., "Quasi-phase-matched parametric interactions in proton-exchanged lithium niobate waveguides," *Journal of The Optical Society of America B*, vol. 14, no. 11, pp. 3197-3203, 1997.

[23] D. Castaldini, et al., "Soft-Proton-Exchange Tapers for Low Insertion-Loss LiNbO3 Devices," *Journal of Lightwave Technology*, vol. 25, no. 6, pp. 1588-1593, 2007.

[24] L. Chanvillard, et al., "Soft proton exchange on periodically poled LiNbO3: A simple waveguide fabrication process for highly efficient nonlinear interactions," *Applied Physics Letters*, vol. 76, no. 9, pp. 1089-1091, 2000.

[25] D. Castaldini, "Study, Fabrication and Characterization of Segmented Waveguides for Advanced Photonic Components on Lithium Niobate, a Thesis," PhD Thesis, Università di Bologna, Bologna, Italy, 2006.

[26] L. De Micheli, Ostrowsky, and M. Papuchon, "Fabrication et Caractérisation de Guides PE Présantant une Faible Variation d'Indice et une Excellente Qualité Optique," *J. Optics (Paris)*, vol. 18, no. 3, pp. 139-144, 1987.

[27] F. Pommereau, M. Iost, F. Vollenbroek, and S. Gourrier, "Resist Profile Control of Image Reversal Process in Contact Lithography," vol. 9, pp. 591-594, 1989.

[28] Clariant. Frederick Seitz Materials Research Laboratory, University of Illinois at Urbana-Champaign. [Online]. http://groups.mrl.uiuc.edu/dvh/pdf/AZ5214E.pdf

[29] C. Mach, *Fundamental Principles of Optical Lithography: The Science of Microfabrication*. John Wiley & Sons, Ltd., 2007.

[30] M. E. Solmaz and C. K. Madsen, "Integration of chalcogenide and titanium-diffused lithium-niobate waveguides," *Proceedings of SPIE*, vol. 7579, no. 75790E, pp. 75790E-1-75790E-7, 2010.

[31] A. C. Cino, et al., "Proton Exchange, Anneal Proton Exchange, and Reverse Proton Exchange Waveguides in Er:LiNbO3," *SPIE*, vol. 3280, pp. 152-160, 1998.

[32] M. Abouelleil and F. J. Leonberger, "Waveguides in Lithium Niobate," *Journal of The America Ceramic Society*, vol. 72, no. 8, pp. 1311-1321, 1989.

APPENDIX

EXAMPLE FABRICATION PROCESS FOR APE WAVEGUIDES

- **Pattern Mask Layer**
  - Deposit 200A^{o}+ mask layer (Ti, SiO_2 , etc) on clean wafer
  - Clean Sample
    - Acetone soak, 5min
    - Isopropyl Alcohol soak, 5min
    - N_2 dry
    - Inspect under microscope for clean surface, repeat and use cotton swab if needed
    - 10min dehydration bake @ 130°C
  - Lithography:
    - Spin coat 4000rpm for 40s AZ5214
    - Soft bake (hotplate) 1min @ 125°C
    - For Positive Lithography
      - Align and expose waveguide mask pattern onto sample
        - Target: 60mJ/cm^2, example: expose 10s@6mJ/cm^2
      - Develop 80s in MF 319, or dilute MF312
    - *For Image Reversal only*
      - Align and expose waveguide mask pattern onto sample
        - Target: 60mJ/cm^2, example: expose 10s@6mJ/cm^2
      - *Reversal-bake (hotplate) 1min30s @ 105°C*
      - *Flood expose sample*
        - *Target: 250mJ/cm^2, example: expose 42s@6mJ/cm^2*
      - *Develop 25s in MF 319, or dilute MF312*
    - Hard bake 8min @ 130°C
  - Open Waveguides (wet etch)
    - Etch 60-80s in BHF, or dilute HF 1:30 H_2O. ex: 3mL HF + 90mL H_20
  - Open Waveguides (RIE etch)
    - Same as standard As_2S_3 etch recipe
  - Strip resist
    - Place samples in a 85°C heated AZ300 photostripper bath, 30min and allow to cool.
    - Rinse with DI water.

- **Exchange in Benzoic Acid**
  - Preparation
    - Add 80mL Benzoic Acid (powder) to Pyrex or Teflon beaker and cover with Al foil.
    - Prepare 300mL beaker of water.
    - Connect Teflon thermocouple to hot plate and power on.
    - Set acid beaker in center of plate, and water on plate near edge.
    - Set hot plate to 80°C and set probe in water beaker.

        - The plate will rise above 80°C to heat the water, which will also begin to melt the acid. Stir acid if needed to ensure all power melts (120°C)
        - Remove water beaker from hotplate when acid is liquid. Remove foil from acid beaker.
        - Place fiberglass *koozie* around acid beaker (ensure sample holder is in place), insert thermal probe, and set hot plate to target temperature: 200°C.
    - Exchange
        - When near target temperature, place sample on holder and sit above acid line so that sample heats up (1min).
        - Immerse sample holder, and wrap fiberglass koozie tightly using the wire belt.
        - Exchange protons for 30min @ 200°C
        - Remove belt and pull sample out above acid line (but keep in beaker so it will slowly cool). The acid vapor will melt your tweezers, and the $LiNbO_3$ is fragile. (1min)
        - Remove koozie/holder complexly and allow sample to cool. (5min)
        - Add next sample and repeat. Turn off hot plate if finished.
    - Cleanup
        - Benzoic Acid is solid at room temperature, and will rapidly crystallize when removed from the melt. Drips and spills wipe up with IPA+ beta wipe.
        - Soak samples in IPA (5min) and rub with cotton swab if needed
        - Rinse in IPA and N_2 blow dry.
- Anneal at 350C
    - Preparation
        - Set furnace in ZEC 46 to 90, 90, 90. This should yield a center temperature of 350°C.
        - Allow to heat for 30min..1hr. You may want to Dektak the samples while you wait.
        - Slowly raise sample temperature: place samples on holder/boat and leave at edge of open furnace for 5-10min.
        - Run dry breathing air (20sccm).
        - Use quartz rod to push boat into furnace center and place end cap/ventilation.
    - Anneal for 4hr @ 350°C.
    - Remove end cap and pull boat to open end of furnace.
    - Switch off furnace and allow to cool down.

SOURCE CODE

This section contains the MATLAB source code used for generating plots used in this work.

They can also be used to determine H diffusion behavior prior to FimmWave simulations.

Sections commence with "%%" using cell-mode notation, and are meant to be executed independently.

```
%this code aims to create a bidimensional [H] profile accounting for
%diffusion in the vertical and horizontal directions.  One must first
%determine the initial exchange diffusion coefficient De(T) and exchange
%depth de(T,t).  This de value is used as the height h needed to create the
%2-dimensional concentration profile.
%------------------------------------------------------------------------------------
%% PE initial step Diffusion Coeff De(T), and exchange depth de(T,t)
%comment/uncomment constants from either Almeida or Howerton prior to calcs
clear all, close all;

%***constants from Almeida et al.
Do= 0.48e8; %um^2/hr for Benzoic Acid
Q= 77.4e3; %J/mol
R= 8.314472; %J/(mol*K)
% %***constants from Howerton et al.
% Do= 1.5e8; %um^2/hr for Benzoic Acid
% Q= 79.3e3; %J/mol
% R= 8.314472; %J/(mol*K)

TC=160:260;  %define temperature range of BA melt, deg C
T= TC+273.15; %convert temp to K
De= Do*exp(-Q./(R*T));  %determine exchange diffusion Coeff

plot(TC,De,'linewidth',1.5), grid on
set(gca,'XMinorTick','On','YminorTick','on','LineWidth',1.5);
Title('H^+ Proton Diffusion of Benzoic Acid in x-cut LiNbO_3, (Almeida, 2007)');
xlabel('Temperature \circC'); ylabel('Diffusion Coeff De(T) [\mum^2/h]');
%% PE step depth estimate
t1= 180; %temp deg C
t2= 200;
t3= 220;
te= 1:60;  %time (min)
de1= sqrt(4*De(t1-159)*te/60)
de2= sqrt(4*De(t2-159)*te/60)
de3= sqrt(4*De(t3-159)*te/60)

plot(te,de1,'k',te,de2,'--b',te,de3,':r','linewidth',1.5); grid on
set(gca,'XMinorTick','On','YminorTick','on','LineWidth',1.5);
xlabel('Exchange time [min]'),ylabel('Exchange Depth d_e [\mum]');
title(['Depth of H^+ protons in x-cut LiNbO_3, (Almeida, 2007)']);
legend('180\circC','200\circC','220\circC');

% -----------------------------------------------------------------------------------
%% Anneal Diffusion Coeff Da(T), and depth da(T,t) calcs
% ---------- Almeida findings, Xcut diffusion
clear all, close all;
K= 8.617385e-5; %Boltzman const, [eV/K]
% Dox= 22.0e12;  %x cut diffusion coeff[um^2/h],as reported by Almeida
% Hx= 1.77;  %eV
Dox= 0.27e12;  %x cut diffusion coeff[um^2/h],as reported by Howerton
Hx= 1.44;  %eV

%-------- for Thesis Plot -------------
t= 0:0.1:10; %anneal time range
TC= 350:450; %Temperature range, deg C
TC1= 350;   %Choose 3 temperatures to plot
TC2= 375;
TC3= 400;
T= TC+ 273.15;
T1= TC1+ 273.15;  %temperature [K]
```

```
T2= TC2+ 273.15;  %temperature [K]
T3= TC3+ 273.15;  %temperature [K]
Dx= Dox*exp(-Hx./(K*T));
Dx1= Dox*exp(-Hx/(K*T1));
Dx2= Dox*exp(-Hx/(K*T2));
Dx3= Dox*exp(-Hx/(K*T3));
plot(TC,Dx,'linewidth',1.5), grid on
set(gca,'XMinorTick','On','YminorTick','on','LineWidth',1.5);
set(gca,'xtick',[350 375 400 425 450])
Title(['H^+ Proton Diffusion for Anneal in x-cut LiNbO3, from (Almeida, 2007)']);
xlabel('Temperature [\circC]');ylabel('Anneal Diffusion Coefficient D_a(T) [\mum]');

da1= 2*sqrt(Dx1*t); %anneal depth da(Da,T)
da2= 2*sqrt(Dx2*t); %anneal depth da(Da,T)
da3= 2*sqrt(Dx3*t); %anneal depth da(Da,T)
figure();plot(t,da3,':r',t,da2,'--b',t,da1,'k','linewidth',1.5), grid on
set(gca,'XMinorTick','On','YminorTick','on','LineWidth',1.5);
Title(['H^+ Proton Diffusion Depth for Anneal in x-cut LiNbO3, from (Almeida, 2007)']);
xlabel('Time t[h]');ylabel('Anneal Depth da [\mum]');
legend('400\circC','375\circC','350\circC');

% ---------------------------------------------------------------------------------
%% Bidimensional [H] profile
%Samples are X cut, y propagating.  Diffusion into substrate is taken as x
%direction, and diffusion toward mask borders is in z direction
%need a vector for x and z directions, distribution is a product of the two
clear all, close all;
%-------[ input parameters ]--------------
lambda= 1531e-3; %wavelength [um]
h= 0.4274;  %initial exchange depth [um](same as 'de')
TC= 20;     %anneal temperature [degC]
T= TC+273.15;  %temperature [K]
width= 7;  %mask width [um]
t= 0.05; % diffusion time (hours)
dd= 0.01;  %incremental value for x and z directions

%-------[ Constants]-------------
K= 8.617385e-5; %Boltzman const, [eV/K]
Co= 0.8;  %H proton concentration after initial exchange

Dox= 22e12;  %x cut diffusion coeff[um^2/h],as reported by Almeida
Hx= 1.77;  %eV
Dx= Dox*exp(-Hx./(K*T));  %Dx(T)

Doz= 0.44e12;  %z cut diffusion coeff[um^2/h],as reported by Almeida
Hz= 1.5;  %eV
Dz= Doz*exp(-Hz./(K*T));  %Dx(T)

%------- [calculations based upon input]--------
nsub= sqrt(4.5820- 0.099169/(0.04432-lambda^2) -0.021950*lambda^2); %ne from Sellmier EQ
dn_pp= 0.075;  %wavelength dependent index change for initial PE layer, 1550nm

w= width/2; %divide width by 2
dx= 2*sqrt(Dx*t);
dz= 2*sqrt(Dz*t);
x= 0:dd:(h+dx)*2;
z= -3*w:dd:3*w; %plot 2x the mask width since the H+ also diffuse in y direction
Cx= erf( (h-x)/dx) + erf( (h+x)/dx);
Cz= erf( (w-z)/dz) + erf( (w+z)/dz);

plot(z,Co/2*Cz); title('Diffusion proile in Z direction');
figure();plot(x,Co/2*Cx);title('Diffusion proile in X direction');
```

```
[X,Z]= meshgrid(Cz,Cx);  %make 2 matrices containing repeating rows or columns of the
original vectors so they may be multiplied together to create a final visual of the 2D
index profile
%note these are flipped since the visual x axis represents the crystal z, and visual y
represents crystal x
CC= Co/4*(X.*Z);  %2D concentration profile
Index= nsub+ dn_pp/4*(X.*Z);  %2D index profile

figure();imagesc(CC); axis image %visualize the concentration profile, square pixels
set(gca,'xtick',[0 w/dd 2*w/dd 3*w/dd 4*w/dd 5*w/dd 6*w/dd])
set(gca,'XTickLabel',{'-3w','-2w','-w','0','w','2w','3w'})
% set(gca,'ytick',x2)
% set(gca,'YTickLabel',cs2)
title(['H Concentration Distribution for Mask Window 2w= ',num2str(width),'\mum']);
xlabel([num2str(t),'hour anneal @',num2str(TC),'\circC']);
%now calculate 2D index profile

% surf(z,x,Index) %3d Visualization

n2= max(max(Index));
Dn_max= n2 -nsub;
sprintf('Exchange depth: %fum\nAnneal time: %2.1fh\nVertical Diffusion: %f\nHorizontal
Diffusion: %f\nSubstrate index: %f at %1.3fum\nWG index: %f\nMax index change: %f\nda/de:
%f',h,t,dx+h,dz,nsub,lambda,n2,Dn_max,dx/h)

% -------------------------------------------------------------------------------------
%% alternative index method (Passaro 2002)
%added 17 Feb, 2011
%valid only for C<=0.12
%dn= 0.1623*C
C1= max(max(CC))
dn= (0.3226*C1 + 0.183*C1^2)*exp(-7.14*C1)
%note: this offers a much more reasonable value of delta n close to Xiaomin
%and Mehmet's Ti diffused waveguides of same dimension
```

VITA

Jacob Douglas Webb received his Bachelor of Science degree in electrical engineering at Texas A&M University in December of 2008. He started his master's degree in September of 2009 researching in the Solid State Photonic Signal Processing Group at Texas A&M University, under the supervision of Dr. Christy Madsen. He received his master's degree in May of 2011, and can be reached at the following address: Jacob Douglas Webb, 111A Zachry Engr. Ctr, College Station, TX 77843-3128. His email address is: jdwmr2@neo.tamu.edu.